The Astrophysical Journal, 906:128 (17pp), 2021 January 10 https://doi.org/10.3847/1538-4357/abce61

Impact of a Magnetic Field on Neutrino–Matter Interactions in Core-collapse Supernovae

Takami Kuroda[1,2]
[1] Max-Planck-Institut für Gravitationsphysik, Am Mühlenberg 1, D-14476 Potsdam-Golm, Germany; takami.kuroda@aei.mpg.de
[2] Institut für Kernphysik, Technische Universität Darmstadt, Schlossgartenstrasse 2, D-64289 Darmstadt, Germany
Received 2020 September 16; revised 2020 November 6; accepted 2020 November 25; published 2021 January 18

Abstract

We explore the impact of a magnetic field on neutrino–matter interactions in core-collapse supernovae. We first derive the modified source terms for neutrino–nucleon scattering and neutrino absorption and emission processes in the moment formalism. Then, we perform full relativistic, three-dimensional, magnetorotational core-collapse supernova simulations of a 20 $M_\odot$ star with spectral neutrino transport. Our simulations self-consistently treat the parity-violation effects of weak interaction in the presence of an external magnetic field. The result shows significant global asymmetry, mostly confined in the proto-neutron star, clearly reflecting the magnetic field structure. The asymmetric property arises from two factors: the angle between the neutrino flux and magnetic field, and the term that is parallel to the magnetic field and is also proportional to the deviation of the distribution function of neutrinos from thermal equilibrium. The typical correction value amounts to ∼1% relative to the total neutrino–matter interaction rate for the magnetic field strength of $\sim 10^{15-16}$ G. Although these asymmetric properties do not immediately affect the explosion dynamics, our results imply that they would be significant once the neutrinos diffuse out of the proto-neutron- star core carrying those asymmetries away. We also show that, during our simulation time of ∼370 ms after bounce, our results indicate that the correction value due to the modified inelastic scattering process dominates over that of the modified neutrino absorption and emission process.

Unified Astronomy Thesaurus concepts: Core-collapse supernovae (304); Magnetohydrodynamical simulations (1966); Supernova neutrinos (1666); Supernova dynamics (1664); Radiative magnetohydrodynamics (2009)

1. Introduction

Massive stars heavier than ∼8 $M_\odot$ terminate their lives with a catastrophic collapse of their central core and subsequent diverse phenomena. Some of them are accompanied by a huge explosion called core-collapse supernova (CCSN; see Janka et al. 2016; Müller 2016; Radice et al. 2018 for recent reviews). There are currently two major explosion mechanisms suggested. The first one relies on the complex interplay between neutrinos and the stellar mantle and is considered to account for CCSNe with a canonical explosion energy of $\sim 10^{51}$ erg (≡1 Bethe, 1 B in short). The other is called magnetorotational (MR) explosion, which takes place if the progenitor star rotates sufficiently fast and is also magnetized (Bisnovatyi-Kogan 1970; LeBlanc & Wilson 1970; Meier et al. 1976; Müller & Hillebrandt 1979).

The MR explosion is intrinsically an asymmetric phenomenon. It is characterized by collimated bipolar outflows (Ardeljan et al. 2000; Burrows et al. 2007; Takiwaki et al. 2009; Scheidegger et al. 2010; Winteler et al. 2012; Sawai & Yamada 2016; Bugli et al. 2020; Obergaulinger & Aloy 2020a). However, recent full three-dimensional (3D) magnetohydrodynamics (MHD) simulations also report less collimated, slightly weaker outflows (Mösta et al. 2014; Kuroda et al. 2020; Obergaulinger & Aloy 2020a). The bipolar structure originated from magnetic field amplification taking place mainly along the rotational axis. Strongly amplified magnetic fields eventually eject matter toward the rotational axis. Another aspect of the MR explosion is its relatively high explosion energy compared to the aforementioned neutrino-heating-driven explosion. Depending on the available differential rotational energy of proto-neutron stars (PNSs), the magnetic field can be very efficiently amplified up to the equipartition level, i.e., roughly the same as the differential rotational energy. Due to the efficient conversion, a typically one order of magnitude larger explosion can be achieved in previous MHD CCSN models (Burrows et al. 2007; Takiwaki et al. 2009; Kuroda et al. 2020; Obergaulinger & Aloy 2020a).

The combination of these two aspects makes the MR explosion one plausible mechanism of a subclass of CCSNe called hypernovae (HNs), which observationally presents a high explosion energy of ∼10 B (see, e.g., Nomoto et al. 2006, and references therein) and is also often accompanied by a bipolar explosion (e.g., Ezzeddine et al. 2019). Although the so-called collapsar model (MacFadyen & Woosley 1999) can currently be considered as a promising mechanism of HNe (e.g., Proga et al. 2003; Kumar & Zhang 2015, and references therein), MR explosion is also attracting considerable attention (Metzger et al. 2011). Furthermore, the asymmetric property of MR explosion is also considered as a plausible kick mechanism of a compact object. All CCSNe leave behind a compact object, either a neutron star (NS) or a black hole, and these compact objects are occasionally observed with a proper motion. While observational results of BH kick velocities are still ambiguous (see, e.g., Repetto et al. 2012 for high-velocity cases or Mandel 2016 for counterarguments), those of NSs show significant velocities of several hundreds to $\gtrsim$1000 km s^{-1} (Hobbs et al. 2005; Winkler & Petre 2007).

Such significant proper motion is likely produced during CCSNe via two possible mechanisms (see, e.g., Lai 2001 for a review). The first one is via asymmetric matter motion and the

other is via asymmetric neutrino emission. Regarding the previous mechanism, most of the recent multi-D simulations of CCSNe indicate that the explosion takes place asymmetrically (for both 2D and 3D models; see, e.g., Bruenn et al. 2016; Takiwaki et al. 2016; Müller et al. 2017; O'Connor & Couch 2018; Ott et al. 2018; Pan et al. 2018; Summa et al. 2018; Nagakura et al. 2019; Vartanyan et al. 2019). This is also the case for MHD simulations (Sawai et al. 2008; Scheidegger et al. 2010; Winteler et al. 2012; Mösta et al. 2014; Bugli et al. 2020; Kuroda et al. 2020; Obergaulinger & Aloy 2020a). In addition, there are observational supports for these asymmetric CCSN models (e.g., Katsuda et al. 2018). The asymmetric explosion in these numerical simulations is often dominated by low-order spherical harmonics modes. Then, the central NS is considered to recoil from the conservation of linear momentum, and the estimated kick velocity reaches a few 100 to $\sim$1000 km s^{-1} (Sawai et al. 2008; Wongwathanarat et al. 2013; Janka 2017; Chan et al. 2018; Müller et al. 2019; Nakamura et al. 2019).

Some progenitor stars, particularly low-mass stars, however, show nearly symmetric ejecta, which are inadequate to account for the observed kick velocity (Gessner & Janka 2018). In such cases, asymmetric neutrino emission can be another possible origin of the kick velocity. Analogous to the anisotropic matter ejection, neutrinos exchange momentum with matter and, if the net exchange does not vanish, the PNS is accelerated. While some previous studies report that the acceleration due to anisotropic neutrino emission is minor and can explain the kick velocity of only up to a few 100 km s^{-1} (Wongwathanarat et al. 2013; Tamborra et al. 2014; Gessner & Janka 2018; Müller et al. 2018), Nagakura et al. (2019) report that its effect is moderate due to a self-sustained partial distribution of the electron fraction (Y_e).

The net momentum that the central compact object gains depends on the degree of asymmetry of neutrino emission and also on its duration time. Regarding the former, the lepton-number emission self-sustained asymmetry (LESA; Tamborra et al. 2014; O'Connor & Couch 2018; Glas et al. 2019; Vartanyan et al. 2019) is currently one of the relevant mechanisms to induce the asymmetric neutrino emission. According to Tamborra et al. (2014), the LESA can explain the kick velocity of 100–200 km s^{-1}. The degree of asymmetry of neutrino emission can still increase if we take into account the magnetic field. In the presence of a magnetic field, a global asymmetry could appear as a consequence of parity violation in neutrino–matter interactions, e.g., neutrino scattering on slightly polarized free nucleons due to magnetic field or Landau quantization of free electrons.

There have been several works studying the parity-violation effects of weak interaction in the presence of a magnetic field in CCSNe. Bisnovatyi-Kogan (1993) investigated the influence of magnetic field on β-process and derived a kick velocity between $\sim$100 and $\sim$3000 km s^{-1}. Horowitz & Li (1998) explored the effect of elastic scattering of neutrinos on slightly polarized free neutrons due to a magnetic field and estimated a magnetic field strength B of $\sim 10^{14}$ G to account for the kick velocity of $\sim$250 km s^{-1}. Later, Arras & Lai (1999, hereafter AL99) pointed out the importance of inelasticity in the scattering process on free nucleons and also of the correct treatment of detailed balance of neutrinos in thermal equilibrium. Taking these modifications into account, they formulated the scattering cross section as well as the absorption one and showed that a dipole magnetic field of $\gtrsim 10^{15}$–10^{16} G is required to generate a kick velocity of a few hundred km s^{-1}. Kotake et al. (2005) was the first to implement the effect of parity violation by β-process into the MHD simulation of CCSNe and showed the increase/reduction of the heating rate of $\sim$0.5%. Maruyama et al. (2011, 2012) calculated the neutrino absorption and cross sections in the context of relativistic mean field theory and derived a relatively high magnetic field of $\sim 10^{17}$ G to explain the kick velocity of $\sim$500–600 km s^{-1}. In addition to the NS kick, the parity-violation effect could also contribute to the pulsar spin evolution (Maruyama et al. 2014; Suwa & Enoto 2014).

In this paper, we aim to implement self-consistently the parity-violation effects of weak interactions in the presence of a magnetic field in a full relativistic two-moment (M1) neutrino transport code. For that purpose, we first rewrite the absorption and cross sections described in AL99 in moment formalism. Then, we apply those modified source terms to full 3D-GR, MR core-collapse simulations of a 20 $M_\odot$ star with spectral neutrino transport. We calculate three models: nonrotating nonmagnetized, rotating strongly magnetized, and a supplemental rotating model with ultra-strongly magnetized models. We also update the neutrino opacities following Kotake et al. (2018). Our results clearly show fingerprints of parity violation in weak interaction. Because of the initially dipole-like magnetic field employed, the parity violation results in a global asymmetry mostly with respect to the equatorial plane. Although these asymmetric features do not immediately affect the explosion dynamics, our results imply that they would be significant in the diffusion timescale of neutrinos. In addition, we also show the importance of the modified inelastic scattering process, which has often been omitted in previous literature, relative to the modified neutrino absorption and emission process.

This paper is organized as follows. Section 2 starts with a concise summary of our general relativistic (GR) MHD neutrino transport scheme. In Section 3, we briefly explain the scattering and absorption cross sections in the presence of a magnetic field and also rewrite them to be suitable for a moment formalism. We describe the initial setup of the simulation together with the updated neutrino opacities in Section 4. The main results and detailed analysis of the effects of parity violation are presented in Section 5. We summarize our results and conclude in Section 6. In Appendix A, we prove that the modified scattering term does not violate the lepton-number conservation. Note that the geometrized unit is used in Section 3 unless otherwise stated, i.e., the speed of light, the gravitational constant, and the Planck constant are set to unity, $c = G = h = 1$, and cgs units are used in Section 5. The metric signature is $(-, +, +, +)$. Greek indices run from 0 to 3 and Latin indices from 1 to 3, except ν and ε, which denote neutrino species and energy, respectively.

2. Basic ν-GRMHD Equations

In our full GR radiation-MHD simulations, we solve the evolution equations of metric, MHD, and energy-dependent neutrino radiation. Each of the metric and radiation-MHD parts is solved in an operator-splitting manner, but the system evolves self-consistently as a whole, satisfying the Hamiltonian and momentum constraints. In this paper, we omit showing the evolution equations for the metric and MHD parts, which can be found in our previous papers, Kuroda et al. (2016, 2020).

We only recapitulate our basic neutrino transport equations below.

We solve the evolution equations for the zeroth- E_ε and first-order radiation moments F_ε^α measured by an Eulerian observer, with ε representing the neutrino energy measured in the comoving frame. The evolution equations read (Shibata et al. 2011)

$$\partial_t \sqrt{\gamma} E_\varepsilon + \partial_i \sqrt{\gamma}(\alpha F_\varepsilon^i - \beta^i E_\varepsilon) + \sqrt{\gamma}\alpha \partial_\varepsilon(\varepsilon \tilde{M}_\varepsilon^\mu n_\mu) = \sqrt{\gamma}(\alpha P_\varepsilon^{ij} K_{ij} - F_\varepsilon^i \partial_i \alpha - \alpha S_\varepsilon^\mu n_\mu) \quad (1)$$

and

$$\partial_t \sqrt{\gamma} F_{\varepsilon i} + \partial_j \sqrt{\gamma}(\alpha P_{\varepsilon i}{}^j - \beta^j F_{\varepsilon i}) - \sqrt{\gamma}\alpha \partial_\varepsilon(\varepsilon \tilde{M}_\varepsilon^\mu \gamma_{i\mu}) = \sqrt{\gamma}[-E_\varepsilon \partial_i \alpha + F_{\varepsilon j}\partial_i \beta^j + (\alpha/2) P_\varepsilon^{jk} \partial_i \gamma_{jk} + \alpha S_\varepsilon^\mu \gamma_{i\mu}]. \quad (2)$$

Here, α, β^i, γ^{ij}, and K_{ij} are the lapse function, shift vector, three metric, and extrinsic curvature, respectively. $\gamma \equiv \det(\gamma_{ij})$ is the determinant of the three metric, P^{ij} is the second-order radiation moment measured in the Eulerian frame and is given by an analytic closure relation (see Kuroda et al. 2016), and S_ε^μ is the source term for neutrino–matter interactions. According to Shibata et al. (2011), the four-source term S_ε^μ in the moment formalism can be expressed as

$$S_\varepsilon^\mu = \varepsilon^3 \int d\Omega B(\varepsilon, \Omega)(u^\mu + l^\mu), \quad (3)$$

where $B(\varepsilon, \Omega)$ is the source term for the distribution function of neutrinos $f(\varepsilon, \Omega)$ with Ω representing the angular dependence. l^μ is a unit normal four vector orthogonal to the four velocity u^μ and is also used to obtain the radiation moments by angular integration of the distribution function as follows:

$$(J_\varepsilon, H_\varepsilon^\alpha, L_\varepsilon^{\alpha\beta}) = \varepsilon^3 \int d\Omega (1, l^\alpha, l^\alpha l^\beta) f(\varepsilon, \Omega). \quad (4)$$

J_ε, H_ε^α, and $L_\varepsilon^{\alpha\beta}$ are the zeroth-, first-, and second-order radiation moments measured in the comoving frame, respectively. In the Doppler and redshift terms, $\tilde{M}_\varepsilon^\mu$ is defined by $\tilde{M}_\varepsilon^\mu \equiv M_\varepsilon^{\mu\alpha\beta}\nabla_\beta u_\alpha$, where $M_\varepsilon^{\mu\alpha\beta}$ denotes the third rank moment of the neutrino distribution function (see Shibata et al. 2011 for as more detailed expression). In the next section, we explain how $B(\varepsilon, \Omega)$ is modified in the presence of a magnetic field and then rewrite it using Equation (3) to obtain the modified four-source term which is used in the M1 neutrino transport Equations (1)–(2).

3. Neutrino Source Terms in the Presence of a Magnetic Field

We begin with a brief description of the modified neutrino source term $B(\varepsilon, \Omega)$ in the presence of a magnetic field. We refer the reader to AL99 for a more detailed background. In the following, we focus on the impacts of a magnetic field on the two dominant neutrino–matter interactions inside the PNS: the neutrino–nucleon scattering and the absorption and emission processes on free nucleons. We now explain each process one by one.

3.1. Modified Neutrino–Nucleon Scattering Rate

The neutrino scattering rate on free nucleons $B_{\rm sc}(\varepsilon, \Omega)$ can be written as

$$B_{\rm sc}(\varepsilon, \Omega) = \int d\varepsilon' d\Omega' \frac{d\Gamma}{d\varepsilon' d\Omega'} \times [e^{-(\varepsilon-\varepsilon')/T}(1 - f(\varepsilon, \Omega))f(\varepsilon', \Omega') - (1 - f(\varepsilon', \Omega'))f(\varepsilon, \Omega)]. \quad (5)$$

Here, T is the matter temperature and $d\Gamma/(d\varepsilon' d\Omega')$ is the differential cross section. Variables with a prime denote those of outgoing neutrinos.

Modification of the scattering rate due to the magnetic field appears in the differential cross section $d\Gamma/(d\varepsilon' d\Omega')$ in terms of $\mu_B b$. Here, μ_B and b are the magnetic moment and magnetic field strength, respectively. We use the value $b = \sqrt{b^\alpha b_\alpha}$ for the magnetic field strength with b^α being the comoving four magnetic field. The typical value of $|\mu_B b|$ in CCSNe is $\lesssim \mathcal{O}(10^{-2})$ MeV, even when one considers a strongly magnetized neutron star with $b \sim 10^{15}$ G (magnetar; Duncan & Thompson 1992). Such a value is significantly smaller than the matter temperature $T \gtrsim 10$ MeV, and we can safely ignore the second- or higher-order terms of $\mu_B b$ in the expansion of $d\Gamma/(d\varepsilon' d\Omega')$. Then, it reads (see AL99)

$$\frac{d\Gamma}{d\varepsilon' d\Omega'} = A_0(\varepsilon, \varepsilon', \mu') + \delta A_+(\varepsilon, \varepsilon', \mu', b) l^\alpha \hat{b}_\alpha + \delta A_-(\varepsilon, \varepsilon', \mu', b) l'^\alpha \hat{b}_\alpha, \quad (6)$$

for electron-type neutrino scattering $\nu_e N \rightarrow \nu_e N$, and

$$\frac{d\Gamma}{d\varepsilon' d\Omega'} = A_0(\varepsilon, \varepsilon', \mu') + \delta A_-(\varepsilon, \varepsilon', \mu', b) l^\alpha \hat{b}_\alpha + \delta A_+(\varepsilon, \varepsilon', \mu', b) l'^\alpha \hat{b}_\alpha, \quad (7)$$

for electron-type antineutrino scattering $\bar{\nu}_e N \rightarrow \bar{\nu}_e N$.

Here, A_0 and $\delta A_\pm$ are the zeroth- and first-order terms of the Taylor expansion of $d\Gamma/(d\varepsilon' d\Omega')$ about b. $\hat{b}^\alpha$ is a unit vector parallel to b^α. μ' is the scattering angle between the incoming and outgoing neutrinos. From Equations (6)–(7), one can rewrite the scattering rate $B_{\rm sc}(\varepsilon, \Omega)$ as a sum of the normal scattering rate $B_{\rm sc}^{b=0}(\varepsilon, \Omega)$, which is independent of the magnetic field, and the correction term $B_{\rm sc}^{b\neq 0}(\varepsilon, \Omega)$, which is proportional to b, as

$$B_{\rm sc}(\varepsilon, \Omega) = B_{\rm sc}^{b=0}(\varepsilon, \Omega) + B_{\rm sc}^{b\neq 0}(\varepsilon, \Omega). \quad (8)$$

For reference, the correction terms $\delta A_\pm(\varepsilon, \varepsilon', \mu', b)$ are expressed in cgs units as (AL99):

$$\delta A_\pm(\varepsilon, \varepsilon', \mu', b) = \frac{2\varepsilon'^2 G_F^2 h_V^N h_A^N m_N^2 \mu_B^N b}{\pi q} \times \frac{1}{[\exp(x_0) + 1][\exp(-x_0 - z) + 1]}\left(1 \pm \frac{h_A^N}{h_V^N}\frac{2m_N q_0}{q^2}\right), \quad (9)$$

for scattering on N, where N takes either n (neutron) or p (proton). In Equation (9), G_F is the Fermi constant with its explicit value being $G_F^2 = G_F^2 c/(\hbar c)^4 = 1.55 \times 10^{-33}$ [cm^3 MeV^{-2} s^{-1}]. h_V^N and h_A^N are the neutral nucleon current form factors, and we adopt the same values used in Bruenn (1985) and Kuroda et al. (2016). $\mu_B^N = g_N e\hbar/(2m_N c)$ is the nucleon

magnetic moment with $g_n = -1.913$ and $g_p = 2.793$, $q_0 = \varepsilon - \varepsilon'$, $q = \sqrt{\varepsilon^2 + \varepsilon'^2 - 2\varepsilon\varepsilon'\mu'}$, $x_0 = \frac{(q_0 - q^2/2m_N)^2}{4Tq^2/2m_N} - \frac{\mu_N}{T}$, and $z = q_0/T$. Hereafter, we omit the arguments $(\varepsilon, \varepsilon', \mu', b)$ in $\delta A_\pm$ for simplicity.

3.2. Moment Formalism of the Modified Neutrino–Nucleon Scattering Rate

In the moment formalism, the scattering term reads

$$S^{\alpha}_{\varepsilon,\mathrm{sc}} = S^{\alpha,b=0}_{\varepsilon,\mathrm{sc}} + S^{\alpha,b\neq 0}_{\varepsilon,\mathrm{sc}}, \tag{10}$$

where

$$S^{\alpha,b=0/b\neq 0}_{\varepsilon,\mathrm{sc}} = \varepsilon^3 \int d\Omega B^{b=0/b\neq 0}_{\mathrm{sc}}(\varepsilon, \Omega)(u^\alpha + l^\alpha). \tag{11}$$

For the scattering term without the contribution of a magnetic field $S^{\alpha,b=0}_{\varepsilon,\mathrm{sc}}$, we only take into account the isoenergetic scattering. Here, we note that scattering on free nucleon is not a perfect elastic system, especially when it is not in thermal equilibrium. However, the inelastic correction term is still minor in CCSNe (Wang & Burrows 2020), and furthermore, to maintain consistency with our previous studies, we simply use the isoenergetic kernel this time. It is written as

$$\begin{aligned} S^{\alpha,b=0}_{\varepsilon,\mathrm{sc}} &= \varepsilon^3 \int d\Omega B^{b=0}_{\mathrm{sc}}(\varepsilon, \Omega)(u^\alpha + l^\alpha) \\ &= -\chi^{\mathrm{iso}}_{\varepsilon} H^{\alpha}_{\varepsilon}, \end{aligned} \tag{12}$$

where $\chi^{\mathrm{iso}}_{\varepsilon}$ is expressed in terms of the isoenergetic scattering kernel (see Appendix 2 in Kuroda et al. 2016 for the explicit expression).

Now we move on to how the source term $B^{b\neq 0}_{\mathrm{sc}}(\varepsilon, \Omega)$ can be expressed in the moment formalism. We note that, in the following, the modified source term $S^{\alpha,b\neq 0}_{\varepsilon,\mathrm{sc}}$ arising from the magnetic field fully considers the inelasticity, which is omitted in the term $S^{\alpha,b=0}_{\varepsilon,\mathrm{sc}}$. This is because that the contribution from inelasticity becomes sometime dominant in the final source term $S^{\alpha,b\neq 0}_{\varepsilon,\mathrm{sc}}$. This is particularly true for neutrinos with energy $\varepsilon \lesssim 4T$ ($\sim$10–80 MeV for $T \sim$ 3–20 MeV; see the discussion around Equation (4.31) in AL99), i.e., most neutrinos inside the PNS. Therefore, the inelasticity is crucial in the parity-violation term.

In the following, we consider the neutrino–nucleon scattering. For the antineutrino–nucleon scattering, we simply switch δA_+ and δA_- in the equations below. The first term on the right-hand side of Equation (11), which is parallel to u^α, corresponds to the zeroth-order moment of the source term. Introducing the same notations used in AL99 (see their Equations (4.14)–(4.15)):

$$C(\varepsilon, \varepsilon') = e^{-q_0/T}(1 - f^{\mathrm{eq}}_{\varepsilon}) + f^{\mathrm{eq}}_{\varepsilon} \tag{13}$$

and

$$D(\varepsilon, \varepsilon') = -(e^{-q_0/T} f^{\mathrm{eq}}_{\varepsilon'} + 1 - f^{\mathrm{eq}}_{\varepsilon'}), \tag{14}$$

where $f^{\mathrm{eq}}_{\varepsilon} = 1/(1 + \exp((\varepsilon - \mu_\nu)/T))$ represents the Fermi distribution function of neutrino with μ_ν being the chemical potential, the zeroth-order term becomes

$$\varepsilon^3 \int d\Omega B^{b\neq 0}_{\mathrm{sc}}(\varepsilon, \Omega) u^\alpha = [H^{\beta}_{\varepsilon} a_{1,\beta}(\varepsilon) + 4\pi\varepsilon^3 c_0(\varepsilon)] u^\alpha. \tag{15}$$

Here, we define

$$a_{1,\alpha}(\varepsilon) = 2\pi \hat{b}_\alpha \int d\varepsilon' \varepsilon'^2 D(\varepsilon, \varepsilon') \int d\mu' (\delta A_+ + \mu' \delta A_-) \tag{16}$$

and

$$c_0(\varepsilon) = 2\pi \hat{b}_\alpha \int d\varepsilon' \varepsilon'^2 C(\varepsilon, \varepsilon') \frac{H^{\alpha}_{\varepsilon'}}{4\pi\varepsilon'^3} \int d\mu' (\mu' \delta A_+ + \delta A_-). \tag{17}$$

To derive Equation (15), we approximate the neutrino distribution function after scattering into isotropic and nonisotropic parts as

$$f(\varepsilon', \Omega') \approx f^0_{\varepsilon'} + f^{1,\alpha}_{\varepsilon'} l_\alpha', \tag{18}$$

where $f^0_{\varepsilon'}$ and $f^{1,\alpha}_{\varepsilon'}$ do not have angle dependency. They are related to the zeroth- and first-order radiation moments in the comoving frame as

$$f^0_{\varepsilon} = \frac{J_{\varepsilon}}{4\pi\varepsilon^3} \tag{19}$$

$$f^{1,\alpha}_{\varepsilon} = \frac{3H^{\alpha}_{\varepsilon}}{4\pi\varepsilon^3}. \tag{20}$$

Similarly, the first-order moment of the source term can also be expressed in terms of the radiation moments as

$$\varepsilon^3 \int d\Omega B^{b\neq 0}_{\mathrm{sc}}(\varepsilon, \Omega) l^\alpha = \left[\tilde{L}^{\alpha\beta}_{\varepsilon} a_{1,\beta}(\varepsilon) + \frac{4\pi\varepsilon^3}{3} h^{\alpha\beta} c_{1,\beta}(\varepsilon) \right], \tag{21}$$

where

$$\begin{aligned} c_{1,\alpha}(\varepsilon) = 2\pi \hat{b}_\alpha &\int d\varepsilon' \varepsilon'^2 C(\varepsilon, \varepsilon')(J_{\varepsilon'} - J^{\mathrm{eq}}_{\varepsilon'})/(4\pi\varepsilon'^3) \\ &\times \int d\mu' (\delta A_+ + \mu' \delta A_-). \end{aligned} \tag{22}$$

In the equation,

$$\tilde{L}^{\alpha\beta}_{\varepsilon} = L^{\alpha\beta}_{\varepsilon} - \frac{1}{3} h^{\alpha\beta} J^{\mathrm{eq}}_{\varepsilon}, \tag{23}$$

$$h_{\alpha\beta} = g_{\alpha\beta} + u_\alpha u_\beta, \tag{24}$$

and

$$J^{\mathrm{eq}}_{\varepsilon} = 4\pi\varepsilon^3 f^{\mathrm{eq}}_{\varepsilon}. \tag{25}$$

Consequently, the summation of Equations (15) and (21) yields the final expression of the source term, Equation (11), expressed as

$$\begin{aligned} S^{\alpha,b\neq 0}_{\varepsilon,\mathrm{sc}} = &[H^{\beta}_{\varepsilon} u^\alpha + \tilde{L}^{\alpha\beta}_{\varepsilon}] a_{1,\beta}(\varepsilon) \\ &+ 4\pi\varepsilon^3 u^\alpha c_0(\varepsilon) \\ &+ \frac{4\pi\varepsilon^3}{3} h^{\alpha\beta} c_{1,\beta}(\varepsilon). \end{aligned} \tag{26}$$

In Appendix A, we prove that this source term does not violate the lepton-number conservation.

In our practical calculation, we prepare a table of the following values in advance:

$$A^0(\varepsilon, \varepsilon', \mu_N, T) = \int d\mu' \delta A_\pm(\varepsilon, \varepsilon', \mu', b)/(\mu^N_B b) \tag{27}$$

$$A^1(\varepsilon, \varepsilon', \mu_N, T) = \int d\mu' \mu' \delta A_\pm(\varepsilon, \varepsilon', \mu', b)/(\mu^N_B b), \tag{28}$$

for $\varepsilon(\varepsilon')$, which is the neutrino's energy grid used, and for typical values of the chemical potential of free nucleons μ_N and matter temperature T in CCSNe. In the above equations, we factored out the magnetic field dependence $\mu_B^N b$ from the tabulated value, which can be incorporated later in the simulation from the local value. During the simulation, we interpolate the values $A^{0,1}$ along the μ_N and T directions at each energy grid ε and ε', multiply them by $\mu_B^N b$, and evaluate Equations (16), (17), (22), and (26).

3.3. Modified Charged Current Reactions with Free Nucleons

In this section, we briefly recapitulate how the magnetic field alters the charged current processes ($\nu_e n \rightleftharpoons e^- p$ and $\bar{\nu}_e p \rightleftharpoons e^+ n$) based on AL99. In the presence of the magnetic field, the energy of electrons and positrons is quantized, namely Landau quantization. Due to this quantization, the Fermi–Dirac distribution of final-state electrons and positrons is also affected. According to AL99, the absorptivity $1/\lambda$ is modified due to the external magnetic field as

$$\lambda^{-1} = \lambda_0^{-1}(1 + \epsilon_{\rm mc} l^\alpha \hat{b}_\alpha). \tag{29}$$

Here, λ_0^{-1} is the absorptivity without the influence of a magnetic field. $\epsilon_{\rm mc}$ is the correction factor due to the magnetic field and expressed as

$$\epsilon_{\rm mc} = \epsilon_{\rm mc}(e^-) + \epsilon_{\rm mc}(np), \tag{30}$$

for the reaction $\nu_e n \rightarrow e^- p$, and

$$\epsilon_{\rm mc} = \epsilon_{\rm mc}(e^+) + \bar{\epsilon}_{\rm mc}(np) \tag{31}$$

for the reaction $\bar{\nu}_e p \rightarrow e^+ n$. The correction terms $\epsilon_{\rm mc}(e^-)$ and $\epsilon_{\rm mc}(e^+)$ originated from electrons and positrons at the ground-state Landau level, while $\epsilon_{\rm mc}(np)$ and $\bar{\epsilon}_{\rm mc}(np)$ are from polarized neutrons and protons.

All these terms have a linear dependence on the magnetic field strength b as follows (in cgs units):

$$\epsilon_{\rm mc}(e^-) = \frac{1}{2}\frac{\hbar c e b}{(\varepsilon + Q)^2}\frac{g_V^2 - g_A^2}{g_V^2 + 3g_A^2}, \tag{32}$$

$$\epsilon_{\rm mc}(e^+) = \frac{1}{2}\frac{\hbar c e b}{(\varepsilon - Q)^2}\frac{g_V^2 - g_A^2}{g_V^2 + 3g_A^2}, \tag{33}$$

$$\begin{aligned}\epsilon_{\rm mc}(np) = &\frac{2g_A(g_A + g_V)}{g_V^2 + 3g_A^2}\frac{\mu_B^n b}{T} \\ &- \frac{T}{\varepsilon + Q}\left[1 + \frac{\varepsilon + Q}{T} f_{e^-}(\varepsilon + Q)\right] \\ &\times \left[\frac{2g_A(g_A + g_V)}{g_V^2 + 3g_A^2}\frac{\mu_B^n b}{T} + \frac{2g_A(g_A - g_V)}{g_V^2 + 3g_A^2}\frac{\mu_B^p b}{T}\right],\end{aligned} \tag{34}$$

and

$$\begin{aligned}\bar{\epsilon}_{\rm mc}(np) = &-\frac{2g_A(g_A - g_V)}{g_V^2 + 3g_A^2}\frac{\mu_B^p b}{T} \\ &+ \frac{T}{\varepsilon - Q}\left[1 + \frac{\varepsilon - Q}{T} f_{e^+}(\varepsilon - Q)\right] \\ &\times \left[\frac{2g_A(g_A - g_V)}{g_V^2 + 3g_A^2}\frac{\mu_B^p b}{T} + \frac{2g_A(g_A + g_V)}{g_V^2 + 3g_A^2}\frac{\mu_B^n b}{T}\right].\end{aligned} \tag{35}$$

In the above equations, $g_V = 1$ and $g_A = 1.23$ are the nucleon charged current form factors (Bruenn 1985), $f_x(\varepsilon) = [1 + \exp((\varepsilon - \mu_x)/T)]^{-1}$ represents the Fermi–Dirac distribution function of fermions x with energy ε and chemical potential μ_x, and $Q = m_n - m_p = 1.2935$ MeV is the rest mass difference of the neutron and proton.

From the modified absorptivity $1/\lambda$, the emissivity j can be obtained by

$$j = \lambda^{-1}\exp((\mu_\nu - \varepsilon)/T), \tag{36}$$

with $\mu_{\nu_e} = -\mu_{\bar{\nu}_e} = \mu_e - \mu_p + \mu_n$ being the chemical potential of neutrinos in thermal equilibrium with matter. Then, the collision rate for neutrino absorption and emission processes (nae) becomes

$$B_{\rm nae}(\varepsilon, \Omega) = \kappa[f(\varepsilon, \Omega) - f_\varepsilon^{\rm eq}], \tag{37}$$

with $\kappa = j + \lambda^{-1}$ being the stimulated absorption opacity.

3.4. Moment Formalism of the Charged Current Reaction Including Magnetic Field Correction

Now, analogously to Section 3.2, we evaluate the charged current source term in moment formalism including the correction term due to the magnetic field. After performing the angular integral $\int d\Omega$ of the collision rate

$$S^\alpha_{\varepsilon,\rm nae} = \varepsilon^3 \int d\Omega B_{\rm nae}(\varepsilon, \Omega)(u^\alpha + l^\alpha) \tag{38}$$

for neutrino absorption and emission processes, it results again in a summation of the normal absorption term $S^{\alpha,b=0}_{\varepsilon,\rm nae}$ and correction term $S^{\alpha,b\neq 0}_{\varepsilon,\rm nae}$ as

$$S^\alpha_{\varepsilon,\rm nae} = S^{\alpha,b=0}_{\varepsilon,\rm nae} + S^{\alpha,b\neq 0}_{\varepsilon,\rm nae}. \tag{39}$$

Here

$$S^{\alpha,b=0}_{\varepsilon,\rm nae} = \kappa[(J^{\rm eq} - J)u^\alpha - H^\alpha] \tag{40}$$

$$S^{\alpha,b\neq 0}_{\varepsilon,\rm nae} = \kappa[-\epsilon_{\rm mc}(H^\beta u^\alpha + \tilde{L}^{\alpha\beta})\hat{b}_\beta]. \tag{41}$$

4. Initial Models and Neutrino Opacities

Utilizing our ν-GRMHD code including the parity-violated source term described above, we perform full 3D CCSN simulations of a magnetized rotating star. Numerical setup is essentially the same as that in our previous paper, Kuroda et al. (2020), other than the neutrino opacity. We study the frequently used solar-metallicity model of the 20 $M_\odot$ star "s20a28n" from Woosley & Heger (2007). For the nuclear equation of state (EOS), we use the SFHo of Steiner et al. (2013). The 3D computational domain is a cubic box with 3×10^4 km width in which nested boxes with 10 refinement

levels are embedded. Each box contains 64^3 cells,[3] and the minimum grid size near the origin is $\Delta x = 458$ m. The neutrino energy space ε logarithmically covers from 1 to 300 MeV with 12 energy bins.

We briefly mention the updated neutrino opacities. In Kuroda et al. (2020), we adopted the standard weak interaction set in Bruenn (1985) plus nucleon–nucleon Bremsstrahlung (Hannestad & Raffelt 1998). In this study, however, we use up-to-date neutrino opacities based on Kotake et al. (2018) in addition to the correction terms arising from the external magnetic field described in the previous section. One of the differences is that we replace the electron capture rate on heavy nuclei by the most elaborate one following Juodagalvis et al. (2010). Furthermore, we also take into account the following corrections: inelastic contributions and weak magnetism corrections (Horowitz 2002), the density-dependent effective nucleon mass (Reddy et al. 1999), the quenching of the axial-vector coupling constant (Carter & Prakash 2002; Fischer 2016), many-body and virial corrections (Horowitz et al. 2017), and strangeness contribution to the axial-vector coupling constant (Horowitz 2002). We therefore employ all opacities listed in Table 1 in Kotake et al. (2018) excluding set3 and set4. The source term can now be summarized as

$$S_\varepsilon^\alpha = S_\varepsilon^{\alpha,b=0} + S_\varepsilon^{\alpha,b\neq 0}, \tag{42}$$

with

$$S_\varepsilon^{\alpha,b=0} = S_{\varepsilon,\mathrm{nae}}^{\alpha,b=0} + S_{\varepsilon,\mathrm{sc}}^{\alpha,b=0} + S_{\varepsilon,\mathrm{nes}}^{\alpha} + S_{\varepsilon,\mathrm{tp}}^{\alpha} + S_{\varepsilon,\mathrm{brem}}^{\alpha} \tag{43}$$

$$S_\varepsilon^{\alpha,b\neq 0} = S_{\varepsilon,\mathrm{nae}}^{\alpha,b\neq 0} + S_{\varepsilon,\mathrm{sc}}^{\alpha,b\neq 0}. \tag{44}$$

Here, the subindices "nes," "tp," and "brem" stand for the neutrino–electron inelastic scattering, thermal neutrino pair production and annihilation, and nucleon–nucleon bremsstrahlung, respectively. We note that this paper does not focus on measuring the impact of these up-to-date neutrino opacities currently used, i.e., Equation (43), which will be reported elsewhere (see Kotake et al. 2018 for a detailed 1D comparison).

The original progenitor model "s20a28n" assumes neither rotation nor magnetic field during its evolution phase. We thus artificially add them to the nonrotating progenitor model as follows:

$$u^t u_\phi = \varpi_0^2(\Omega_0 - \Omega), \tag{45}$$

for the rotational profile, and

$$A_\phi = \frac{B_0}{2}\frac{R_0^3}{r^3 + R_0^3} r\sin\theta, \tag{46}$$

$$A_r = A_\theta = 0, \tag{47}$$

for the magnetic field in the form of a vector potential. Here, $u_\phi \equiv \sqrt{u_x^2 + u_y^2}$ and ϖ_0 and Ω_0 indicate the size and angular frequency of a rigidly rotating central cylinder, respectively. B_0 and R_0 represent the magnetic field strength at the center and the size of the central sphere with a uniform magnetic field, respectively. (r, θ, ϕ) denote the usual coordinates in the spherical polar coordinate system. By defining the vector potential on the numerical cell edge and taking their curl $\boldsymbol{B} = \nabla \times \boldsymbol{A}$, the magnetic field defined on the numerical cell surface automatically satisfies the solenoidal constraint. These rotational and magnetic field profiles are identical to those used in our previous paper, Kuroda et al. (2020).

We set $\varpi_0 = R_0 = 10^8$ cm, corresponding roughly to the iron core size at the precollapse stage. We calculate three models with varying (Ω_0[rad s^{-1}], B_0[G]) as (0, 0), (1, 10^{12}), and (1, 10^{13}), hereafter labeled R0B00, R1B12, and R1B13, respectively. The angular frequency $\Omega_0 = 1$ rad s^{-1} is very reasonable compared to that of a rotating 20 $M_\odot$ model in Heger & Langer (2000) that gives $\Omega_0 \sim 3$ rad s^{-1}. Regarding the magnetic field strength inside the iron core at the precollapse stage, there is currently no constraint from the observational and stellar evolution calculation sides. The value $B_0 = 10^{12}$ G in model R1B12 is widely used in most previous magnetorotational explosion (MRE) simulations (Burrows et al. 2007; Takiwaki et al. 2009; Scheidegger et al. 2010; Mösta et al. 2014; Bugli et al. 2020; Kuroda et al. 2020; Obergaulinger & Aloy 2020a) and can be a reference case. On the other hand, $B_0 = 10^{13}$ G is enormously strong and might be unrealistic. We, however, calculate such an ultra-strongly magnetized model to measure the impact of magnetic field on the neutrino–matter interactions more easily, because the source terms Equations (26) and (41) have a linear dependence on the magnetic field strength b.

5. Results

In this section, we present the results of our simulations. We begin with a detailed explanation of the explosion dynamics of our fiducial model R1B12 and then compare three models including neutrino profiles. Afterward, we discuss our main results on the actual impact of magnetic field on the neutrino–matter interaction and its possible effects on the dynamics. As we will show, we see global asymmetric features in the neutrino–matter interactions appearing in the PNS that are closely correlated with the magnetic field structure. Therefore, we consider that understanding the magnetohydrodynamics inside the PNS is essential to explain those asymmetric features.

5.1. Explosion Dynamics

We explain first the dynamical evolution of our fiducial model R1B12. Its evolution is essentially the same as in our previous study employing the same initial condition (model R1B12 in Kuroda et al. 2020), and the bipolar outflow is launched soon after bounce. Figure 1 shows the volume-rendered 3D entropy structure for model R1B12 at two different time slices $t_{\mathrm{pb}} = 183$ ms (top-left panel) and 367 ms (top right), where t_{pb} represents the postbounce time, and 2D contours of entropy (bottom left) and plasma $\beta(\equiv P_{\mathrm{mag}}/P_{\mathrm{gas}})$, which is the ratio of magnetic to gas pressure, in logarithmic scale (bottom right) at the final simulation time. The white vertical line in the top panels indicates the length scale and is also parallel to the rotational axis (z-axis). There are three mini panels in the bottom two panels. Each mini panel shows a 2D slice on $y = 0$ (mini panel (a)), $x = 0$ (b), and $z = 0$ (c) planes. From the figure, we see a clear bipolar shock structure which continuously expands without stalling. The size of the shock surface increases from $\sim$1000 to $\gtrsim$4000 km for the time

[3] In Kuroda et al. (2020), there is a typo in the number of grids. It should be 64^3 cells that cover each level of nested structure, i.e., the same resolution as in this study.

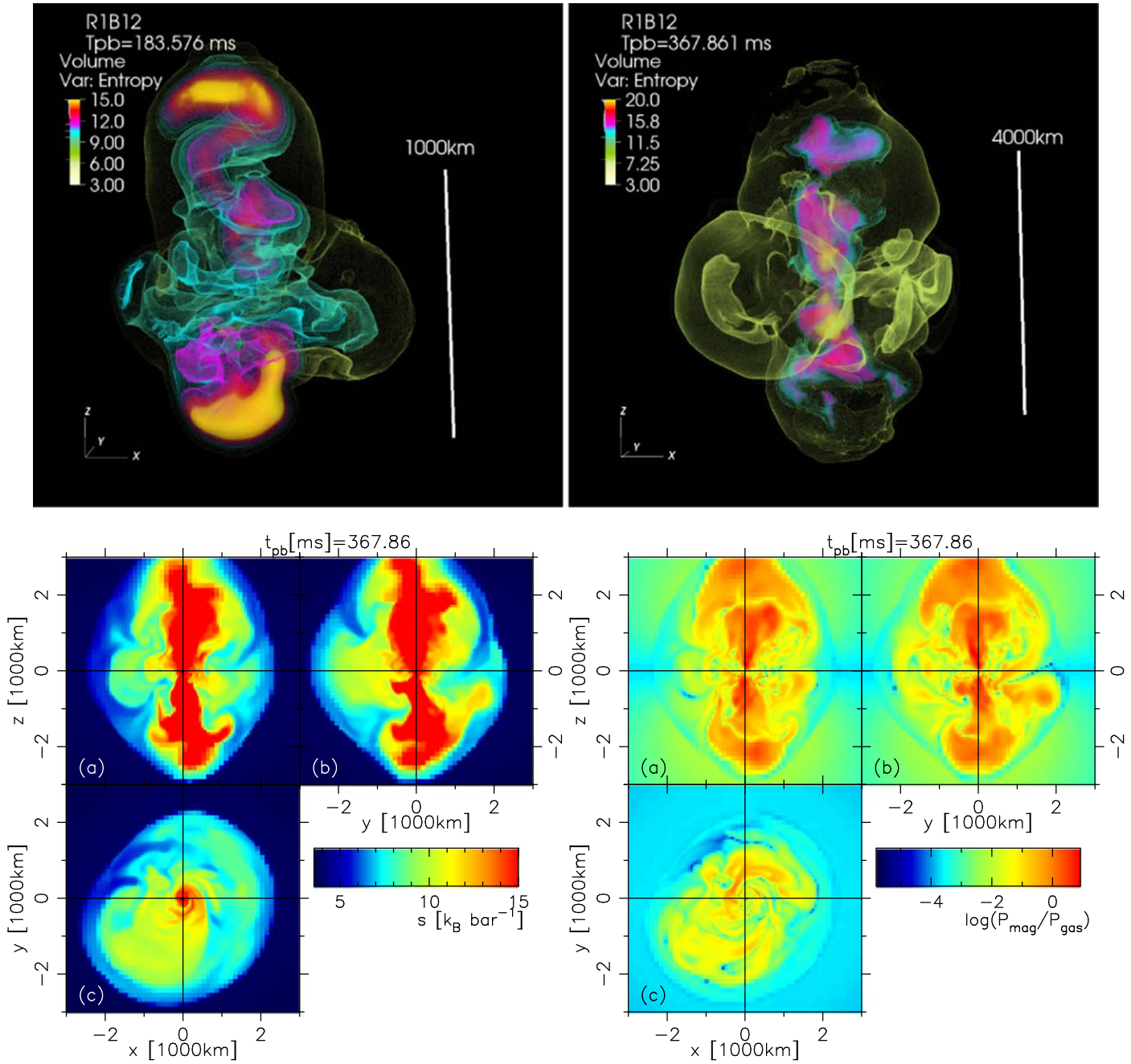

Figure 1. Top: the volume-rendered entropy for model R1B12 at two different time slices $t_{\rm pb} = 183$ ms (left panel) and 367 ms (right). The white vertical line indicates the length scale and is also parallel to the rotational axis (z-axis). Note that the entropy range differs in each panel. Bottom: we depict 2D contours of the entropy (left) and plasma β (right) in logarithmic scale at the final simulation time of $t_{\rm pb} = 316$ ms. There are three mini panels in the bottom panels. Each mini panel shows a 2D slice on the $y = 0$ (mini panel (a)), $x = 0$ (b), and $z = 0$ (c) planes.

interval of ∼180 ms. Model R1B12 is thus considered to be entering the shock runaway phase directly after bounce.

Its explosion morphology exhibits a clear bipolar-like structure with a slight asymmetry with respect to the equatorial plane. From the bottom mini panels (a) and (b), the expansion toward the positive z-axis is more energetic than that in the negative direction. The bipolar structure consists of high-entropy ejecta, and the entropy increases with time. The forefront of the bipolar jet shows the highest entropy of $s \sim 15\,k_{\rm B}$ baryon^{-1} at $t_{\rm pb} \sim 183$ ms, while the vicinity at the base of jets shows the highest value exceeding $s \sim 20\,k_{\rm B}$ baryon^{-1} at $t_{\rm pb} \sim 367$ ms (yellowish region in the top-right panel). Furthermore, the jet barycenter shows a clear displacement from the rotational axis, like a helical structure seen in the top-left panel, indicating the appearance of the kink instability (e.g., Begelman 1998). This is consistent with previous full 3D MHD CCSN simulations (Mösta et al. 2014; Kuroda et al. 2020). From the bottom-right panel, we see that the magnetic pressure dominates over the gas pressure inside the outflow (red region), indicating that the MR-driven explosion occurs in this model.

Regarding the north–south asymmetry seen in the explosion morphology, one might expect that it could be caused by the parity-violation effects. We, however, consider that the

asymmetry appearing during our simulation time, i.e., the early postbounce phase of $t_{\rm pb} \lesssim$ a few 100 ms, is unlikely due to the parity-violation effects of weak interactions, but mostly due to MHD effects. In our previous study (Kuroda et al. 2020), which did not take into account the parity-violation effects, the north–south asymmetry was also found. In the literature, we introduced a combination of the $m = 1$ rotational instability and the MHD kink instability as one possible explanation of the north–south asymmetry. By comparing the degree of the asymmetry between this and previous studies, we recognize that there is no significant difference, especially in the initial postbounce phase of $t_{\rm pb} \lesssim 100$ ms, during which the parity-violation effects are particularly strong (explained in Section 5.2). More precisely, the corresponding normalized mode amplitudes of the spherical polar expansion of the shock surface $A_{\ell m}$ read $\sim$0.05% in both studies for $(\ell, m) = (1, 0)$. We thus consider that the parity-violation effects play a subdominant role, at least in the early postbounce phase, in forming the shock morphology.

On the equatorial plane, a clear $m = 1$ nonaxisymmetric structure becomes prominent (see mini panels (c)). Along the equatorial plane, both continuous mass accretion, with low entropy $s \lesssim 5\ k_{\rm B}$ baryon^{-1}, and ejection, with relatively high $s \sim 10\ k_{\rm B}$ baryon^{-1}, simultaneously take place. Furthermore, from mini panel (c) in the bottom-right panel, we find the gas pressure being dominant in most of the regions, i.e., the magnetic field does not play a leading role in the shock expansion. We thus argue that the shock expansion is significantly aided by rotation in the equatorial region (see Nakamura et al. 2014; Takiwaki et al. 2016; Summa et al. 2018 for the rotation-supported 3D CCSN models and also Kuroda et al. 2020 with a magnetic field).

We also calculate a supplement model R1B13, which adopts a one order of magnitude larger initial magnetic field, to focus on its possibly more emphasized parity-violation effects. Thus, we leave its detailed explanation of (magneto)hydrodynamics to Appendix B. Roughly speaking, this model also exhibits a very energetic shock expansion immediately after bounce. However, the magnetic field structure and the entropy structure within the shocked region are significantly different from those in model R1B12. They do not show a simple bipolar-like structure compared to those in model R1B12, but a slightly complicated structure.

Figure 2 presents the time evolution of the shock radius $R_{\rm shock}$ in the top panel and of the diagnostic explosion energy $E_{\rm exp}$ in the bottom, where we use the same definition for $E_{\rm exp}$ as Kuroda et al. (2020). In the top panel, we plot the maximum (thick line) and averaged shock radii (thin) for all models. We multiply the lines of $R_{\rm shock}$ for model R0B00 (black lines) by 10 to show them more clearly. We find that the model R0B00, which assumes neither rotation nor magnetic field initially, does not exhibit shock revival during our simulation time of $\sim$500 ms after bounce. This is consistent with our previous study, Kuroda et al. (2020). We thus argue that the up-to-date neutrino opacities do not drastically change the explosion dynamics. Therefore, in the bottom panel, we omit the line for model R0B00 because its explosion energy is essentially zero.

The time evolution of shock radii presents a rapidly expanding shock surface in model R1B13 immediately after bounce (red lines). The maximum shock radius reaches $R = 1000$ km at $t_{\rm pb} \sim 70$ ms. During the same period, $E_{\rm exp}$ increases drastically initially, reaches its maximum $\sim 6 \times 10^{50}$ erg at $t_{\rm pb} \sim 20$ ms, and declines afterward. The contribution of each energy to the total diagnostic explosion energy at $t_{\rm pb} = 20$ ms is as follows: the magnetic energy $\sim 10^{51}$ erg, the internal energy $\sim 4 \times 10^{50}$ erg, the radial kinetic energy $\sim 2 \times 10^{50}$ erg, and the rotational kinetic energy $\sim 2 \times 10^{50}$ erg. The prompt explosion is thus mainly supported by the magnetic field. The decline seen in $E_{\rm exp}$ after $t_{\rm pb} \sim 20$ ms is mostly due to the decrease of the magnetic energy in the unbound region, while in model R1B12 (blue lines) the shock front shows a mild expansion initially ($t_{\rm pb} \lesssim 120$ ms) and subsequently becomes faster than that of model R1B13. Its averaged shock radius (thin blue line) exceeds that of model R1B13 at $t_{\rm pb} \sim 310$ ms. The explosion energy $E_{\rm exp}$ in model R1B12 increases at $t_{\rm pb} \sim 100$ ms and then plateaus around the value of $\sim 10^{50}$ erg. The shock and explosion energy evolution in models R1B12 and R0B00 are quantitatively in good agreement with our previous report (Kuroda et al. 2020), which employed the same initial condition except the neutrino opacity set.

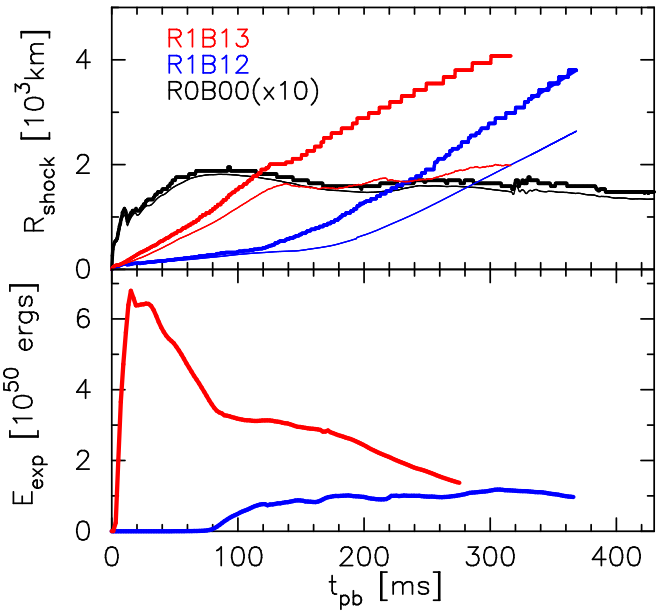

Figure 2. Top: time evolution of maximum (thick lines) and averaged shock radii (thin) for all models. To show more clearly the lines of model R0B00, we multiply them by 10. Bottom: we plot the diagnostic explosion energy. Because $E_{\rm exp}$ of model R0B00 is essentially zero, we omit plotting it.

We next explain the different explosion dynamics seen in the two magnetized models, particularly focusing on the reason why the initially less magnetized model R1B12 eventually shows a more energetic explosion. Figure 3 depicts the mass inflow ($\dot{M} < 0$) and outflow rates ($\dot{M} > 0$) by the solid lines and the total mass accretion rate by the dashed–dotted line. The color represents either model R1B13 (red) or R1B12 (blue). The rate is measured at $R = 100$ km so that we can encompass the base of the MHD outflow located at $R \sim$ a few 10 km. In model R1B12 (blue lines), the absolute values of both the mass inflow and outflow rates are significantly larger than those of model R1B13 (red). Especially after $t_{\rm pb} \gtrsim 40$ ms, the mass inflow rate in model R1B12 shows a larger value of $\sim 1\ \dot{M}_{\odot}\ {\rm s}^{-1}$ from the one in R1B13. At the same time, a large amount of mass ejection also takes place in model R1B12, resulting in a moderate difference between the total mass accretion rates of the two models (dashed–dotted lines). The smaller mass inflow rate in model R1B13 is a consequence of the stronger explosion

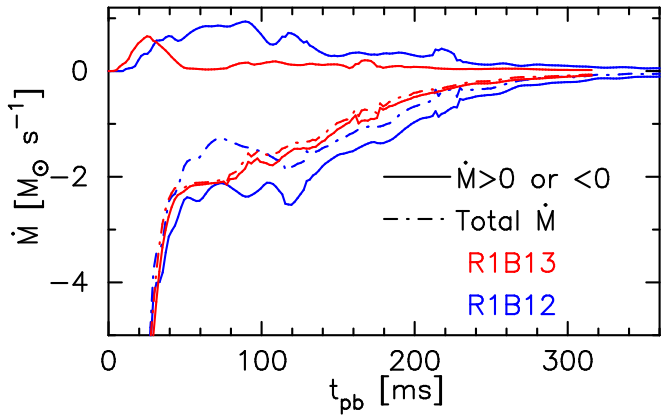

Figure 3. We plot the mass inflow ($\dot{M} < 0$) and outflow rate ($\dot{M} > 0$; solid lines) and the total accretion rate (dashed–dotted) measured at $R = 100$ km for models R1B13 (red) and R1B12 (blue).

taking place immediately after bounce. As we have already explained, an enormously strong shock wave, which is mainly supported by the magnetic pressure, is launched shortly after bounce. The shock propagates outward in all directions and suppresses the subsequent mass accretion onto the central engine of the MHD outflow. Lower accretion produces less liberation gravitational potential energy, and thus, the strong bipolar flow is not continuously supported. This is the reason for the weaker shock wave and also the different magnetic field and entropy configurations eventually seen in model R1B13.

On the other hand, the shock propagates significantly slower in model R1B12 at the initial postbounce phase, which allows the development of nonaxisymmetric matter motion, e.g., a one-armed spiral pattern. Indeed, the ratio of rotational to gravitational potential energy reaches a few percent in model R1B12, while it is significantly smaller, ∼0.5%, in R1B13. The spiral pattern then produces a flow channel through which a noticeable amount of mass accretion takes place as we have shown in the bottom panels of Figure 1.

5.2. North–South Asymmetry of Neutrino–Matter Interaction

In this section, we discuss the modified neutrino–matter interactions in the presence of a magnetic field and their actual impact on the dynamics. We begin with a brief explanation of the overall picture of neutrino signals. The nonexplosion model R0B00 basically shows the highest luminosity and mean energy in all flavors of neutrinos, while the rotating magnetized models R1B12 and R1B13, which explode shortly after bounce, show rather lower values. Roughly speaking, such a feature is consistent with our previous study (Kuroda et al. 2020) and also with those in recent studies with detailed neutrino transport (Müller et al. 2017; O'Connor & Couch 2018; Summa et al. 2018; Vartanyan et al. 2019).

To see more precisely how the modified neutrino–matter interactions lead to asymmetric properties, particularly with respect to the equatorial plane, we depict several quantities in Figure 4. Here, we introduce several quantities as follows: the change rate of the electron fraction $\Gamma_e (\equiv \partial Y_e/\partial t)$ independent from ($\Gamma_e^{b=0}$) and dependent on ($\Gamma_e^{b\neq 0}$) the magnetic field:

$$\Gamma_e^{b=0/b\neq 0} = \frac{\alpha\sqrt{\gamma}}{n_{\rm b}} \int \frac{d\varepsilon}{\varepsilon} S_\varepsilon^{\mu,b=0/b\neq 0} u_\mu, \tag{48}$$

where $n_{\rm b}$ is the number density of baryons, the energy deposition rate $Q_{\rm nae}^{b\neq 0}$ originating from the modified neutrino absorption and emission process,

$$Q_{\rm nae}^{b\neq 0} = \alpha\sqrt{\gamma} \int d\varepsilon S_{\varepsilon,{\rm nae}}^{\mu,b\neq 0} n_\mu, \tag{49}$$

the energy deposition rate $Q_{\rm sc}^{b\neq 0}$ originating from the modified inelastic neutrino–nucleon scattering process,

$$Q_{\rm sc}^{b\neq 0} = \alpha\sqrt{\gamma} \int d\varepsilon S_{\varepsilon,{\rm sc}}^{\mu,b\neq 0} n_\mu, \tag{50}$$

the energy deposition rate $Q_{\rm tot}$ originating from normal neutrino–matter interactions (see Equation (43)),

$$Q_{\rm tot} = \alpha\sqrt{\gamma} \int d\varepsilon S_\varepsilon^{\mu,b=0} n_\mu, \tag{51}$$

the torque τ_ϕ that the fluid element gains due to the modified source term $S_\varepsilon^{\alpha,b\neq 0}$,

$$\tau_\phi = -\alpha\sqrt{\gamma}\varpi \int d\varepsilon S_\varepsilon^{\mu,b\neq 0} \gamma_{y\mu}, \tag{52}$$

where $\varpi = \sqrt{x^2 + y^2}$ is the distance from the rotational axis, and the z component of the force acting on the fluid element f_z due to the modified source term $S_\varepsilon^{\alpha,b\neq 0}$,

$$f_z = -\alpha\sqrt{\gamma} \int d\varepsilon S_\varepsilon^{\mu,b\neq 0} \gamma_{z\mu}. \tag{53}$$

We also introduce the following ratios to assess the relative impact of the modified neutrino–matter interactions to the normal ones as

$$\gamma_e = \frac{\Gamma_e^{b\neq 0}}{|\Gamma_e^{b=0}|} \tag{54}$$

$$q_{\rm nae/sc} = \frac{Q_{\rm nae/sc}^{b\neq 0}}{|Q_{\rm tot}|}. \tag{55}$$

We note that we take the absolute value of the denominator for later convenience. Using these quantities, we show in Figure 4 (mini panel (a)) the z component of magnetic field B_z, (b) the ϕ component of the magnetic field B_ϕ, (c) $\Gamma_e^{b\neq 0}$, (d) $\log \gamma_e$, (e) $\log q_{\rm nae}$, (f) $\log q_{\rm sc}$, (g) $\log \tau_\phi$, and (h) $\log f_z$. All panels show the contours on the $y = 0$ plane for model R1B12 at $t_{\rm pb} = 65$ ms. We also plot the mean gain radius by a red circle in panels (c)–(h) for reference.

In panel (a), we see that B_z is positive inside the PNS with its value being $\sim 10^{15}$ G in both hemispheres. This is mostly due to the compression of n initial uniform or dipole-like magnetic field aligning with the z-axis inside $\varpi \lesssim 1000$ km. B_ϕ shows a clear asymmetry with respect to the equatorial plane, and the northern ($z > 0$) and southern ($z < 0$) hemispheres possess negative and positive B_ϕ, respectively. Within the PNS, the toroidal magnetic field strength reaches $\sim 10^{15}$ G. Reflecting the nonisotropic magnetic field, the change rate of the electron fraction $\Gamma_e^{b\neq 0}$ also shows a clear north–south asymmetry in panel (c). Here we note that $\Gamma_e^{b\neq 0}$ is affected only by the modified neutrino absorption and emission process (Equation (41)), because the (modified) scattering process in Equation (26) does not change the electron number at all as proved in Appendix A. Panel (c) shows that the northern hemisphere deleptonizes more. This can be understood from Equation (41). Using the orthogonality condition $\tilde{L}^{\alpha\beta} u_\alpha = 0$,

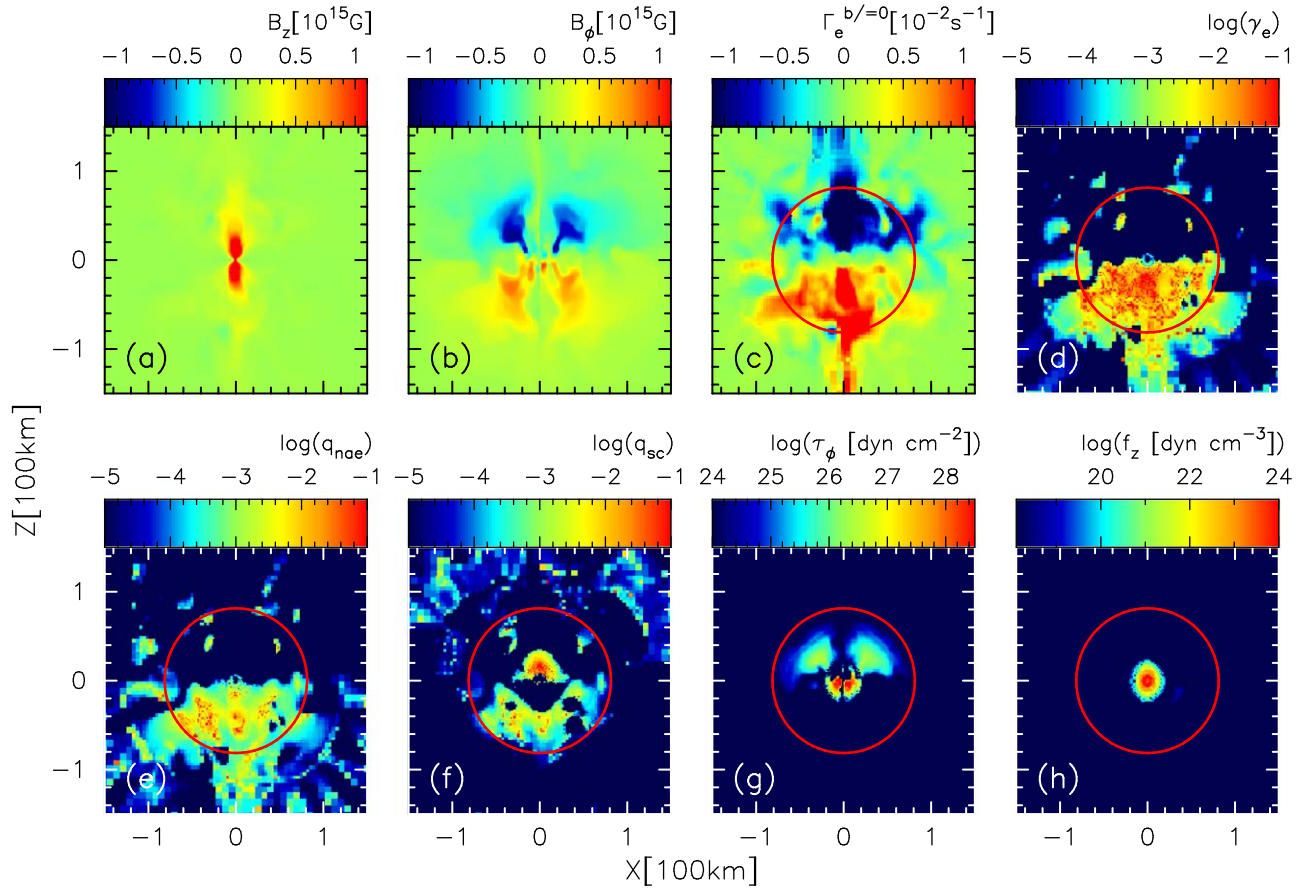

Figure 4. We show (a) the z component of the magnetic field B_z in units of 10^{15} G, (b) the ϕ-component of magnetic field B_ϕ in units of 10^{15} G, (c) $\Gamma_e^{b\neq 0}$ in units of s^{-1}, (d) $\log \gamma_e$, (e) $\log q_{\rm nae}$, (f) $\log q_{\rm sc}$, (g) the torque per volume that the fluid element gains τ_ϕ dyn cm^{-2} in logarithmic scale, and (h) the force acting on the fluid element per volume f_z dyn cm^{-3} in logarithmic scale. Concerning the values in panels (d)–(h), where the values are shown in logarithmic scale, we do not take their absolute values, and the negative values are simply cut off at the minimum value indicated in dark blue. The figure is for model R1B12 at $t_{\rm pb} = 65$ ms on the $y = 0$ plane.

$\Gamma_e^{b\neq 0}$ is expressed as

$$\Gamma_e^{b\neq 0} = \alpha\sqrt{\gamma}\int \frac{d\varepsilon}{\varepsilon} S_\varepsilon^{\mu,b\neq 0} u_\mu = \alpha\sqrt{\gamma}\int \frac{d\varepsilon}{\varepsilon}\kappa\epsilon_{\rm mc} H^\beta \hat{b}_\beta. \quad (56)$$

$\epsilon_{\rm mc}$ (Equation (30)) is usually negative due to $g_V^2 - g_A^2 < 0$ and also in the degenerate limit of electrons $f_{e^-} \sim 1$. Therefore, the sign of $\Gamma_e^{b\neq 0}$ is determined by the angle between the direction of the flux of neutrinos H^β and that of magnetic field $\hat{b}_\beta$. Because the H^β of ν_e is usually oriented radially outward inside the PNS, i.e., $H^i \sim (H^r, 0, 0)$, the toroidal magnetic field B_ϕ does not contribute to $\Gamma_e^{b\neq 0}$ as they are mutually orthogonal. The remaining magnetic field component B_z is pointing positive z direction from panel (a). As a consequence, the northern hemisphere, where $H^\beta\hat{b}_\beta > 0$, $\Gamma_e^{b\neq 0}$ becomes negative, while the southern hemisphere analogously shows a positive $\Gamma_e^{b\neq 0}$.

Panel (d) indicates how large is the contribution of $\Gamma_e^{b\neq 0}$ to the total deleptonization rate $|\Gamma_e^{b=0}|$. Here, we note that most of the northern hemisphere displays a dark blue region simply because we cut off the negative value to emphasize the north–south asymmetry. However, it actually has a similar value to the southern hemisphere, but with a different sign. We also mention that the deleptonization rate $\Gamma_e^{b=0}$, which is free from the influence of the magnetic field, shows a nearly perfect symmetry with respect to the equatorial plane. From panel (d), the value of γ_e in the southern hemisphere reaches several percent, which is also the same for the northern hemisphere. The parity violation in the weak interaction due to the external magnetic field thus can potentially produce a significant partial distribution of Y_e in the PNS, which will also be discussed later. As $\Gamma_e^{b\neq 0}$ in panel (c) shows $\sim\pm 0.01$ s^{-1} along the rotational axis, if the parity-violation effect lasts $\sim$100 ms, the cumulative change reaches $\delta Y_e \sim \pm 10^{-3}$. In previous studies, Tamborra et al. (2014) reported the existence of the LESA (see also, e.g., O'Connor & Couch 2018; Powell & Müller 2019; Vartanyan et al. 2019), which originated from a partial distribution of Y_e in the PNS convection zone ($r \sim 25$ km). In their subsequent paper (Glas et al. 2019), they explained the origin of the partial distribution of Y_e, dominated mainly by the $l = 1$ mode, by the PNS convection. Aside from the PNS convection, our study shows for the first time that the neutrino–matter interactions in the presence of a strong external magnetic field can be another possible mechanism to produce a partial distribution of Y_e.

Next, we evaluate the impact of heating and cooling rates contributed by the modified charged and neutral current reactions in panels (e) and (f), respectively. Comparing panels

(d) and (e), they show similar patterns as expected, i.e., $Q_{\rm nae}^{b\neq 0}$ has basically the same sign as $\Gamma_e^{b\neq 0}$. Panel (e) indicates a larger heating and cooling rate in the southern and northern hemispheres, respectively. Employing essentially the same initial magnetic field but with various strengths, Kotake et al. (2005) also reported the excess of neutrino heating in the southern hemisphere. Our result is thus qualitatively consistent with theirs. In addition, Kotake et al. (2005) show a relative contribution of $Q_{\rm nae}^{b\neq 0}$ to the total heating/cooling rate $Q_{\rm tot}$ of the order of $\sim$0.1%, which is also in good agreement with ours. The excess/reduction of the energy exchange rate above the gain radius is several 0.1% from panel (e).

Regarding $Q_{\rm sc}^{b\neq 0}$ (or $q_{\rm sc}$), $Q_{\rm sc}^{b\neq 0}$ again shows a clear asymmetric feature in panel (f). Inside the central region with $r \lesssim 30$ km, the northern and southern hemispheres show the excess of neutrino heating and cooling, respectively. Meanwhile, the sign inverts around $r \sim 40$ km. The reason for the asymmetry and sign inversion can be understood as follows. From Equation (26) and also using the fact that $a_{1,\alpha}$ is proportional to b_α (see Equation (16)), we find that $S_{\varepsilon,\rm sc}^{\alpha,b\neq 0}$ consists of two parts. One is proportional to $H^\beta b_\beta$ and the other is proportional to $|\tilde{L}| \sim J - J^{\rm eq}$, namely the deviation of the neutrino distribution function from thermal equilibrium, as

$$S_{\rm sc}^{\alpha,b\neq 0} \propto H^\beta b_\beta u^\alpha + \frac{J - J^{\rm eq}}{3} b^\alpha. \tag{57}$$

Here, we use the relation $h^{\alpha\beta}b_\beta = b^\alpha$. The source term for the zeroth radiation moment $Q_{\rm sc}^{b\neq 0}$ is then rewritten by taking the norm with n_α as

$$\begin{aligned} Q_{\rm sc}^{b\neq 0} &\sim \int d\varepsilon S_{\rm sc}^{\alpha,b\neq 0} n_\alpha \\ &\propto \int d\varepsilon \left(-WH^\beta b_\beta - \frac{J - J^{\rm eq}}{3} B^i u_i \right). \end{aligned} \tag{58}$$

Inside the deep PNS core, the radiation field and matter velocity exhibit a nearly isotropic structure, i.e., $l = 0$ with l denoting the degree of spherical harmonics, while the magnetic field shows a uniform (dipole-like) field for our initial condition, i.e., $l = 1$. As a consequence, both the first and second terms, which depend on the angle between the magnetic field and H^β and u_i, respectively, basically change their signs between the northern and southern hemispheres. This is the reason for the asymmetric structure with respect to the equatorial plane. The sign inversion seen at $r \sim 40$ km depends simply on which term of the integrand becomes the dominant term and cannot be inferred a priori. It is also noteworthy that $Q_{\rm sc}^{b\neq 0}$ has a value comparable to or even a slightly larger than $Q_{\rm nae}^{b\neq 0}$. This fact indicates the importance of the modified neutrino–nucleon scattering term due to the magnetic field that has often been omitted in previous studies on the parity-violation effects in CCSNe (Kotake et al. 2005; Suwa & Enoto 2014; Dobrynina & Ognev 2020).

We also discuss the parity-violation effects on the angular and linear momentum transfer. In panel (g), we show the torque that the PNS gains. It is obvious that the PNS core $r \lesssim 30$ km is subjected to torsional stress, and the northern and southern hemispheres spin down and up, respectively. A possibility of such torsional effect has been already discussed in Maruyama et al. (2014), in which a region where the direction of rotation is the same as that of the magnetic field shows a spin deceleration. Our result thus supports their discussion. However, because they considered only the effect of an absorption process influenced by the magnetic field, our result with both scattering and absorption processes considered shows a more complicated spin deceleration or acceleration profile. Finally, from panel (h), we find that linear momentum transfer occurs mostly in the PNS core. At there, f_z shows a positive value in both hemispheres without asymmetry with respect to the equatorial plane. It indicates that the whole PNS core can be kicked toward north at this time. The symmetric structure seen in f_z can be understood like below. Here we mention that the main contribution to the momentum transfer comes from the scattering term $S_{\varepsilon,\rm sc}^{\alpha,b\neq 0}$, and we thus focus on this term. Using Equation (57), f_z can be expressed as

$$\begin{aligned} f_z &\sim -\int d\varepsilon S_{\rm sc}^{\alpha,b\neq 0} \gamma_{z\alpha} \\ &\propto -\int d\varepsilon \left(H^z b_z u_z + \frac{J - J^{\rm eq}}{3} b_z \right), \end{aligned} \tag{59}$$

where we take only the z component for α when we move from the first line to the second. This is because the dominant magnetic field component is $B_z \sim b_z (>0)$ around the rotational axis in the PNS core. Bearing in mind that the radiation field and matter are roughly isotropic inside the PNS core, $H^z u_z$ and $J - J^{\rm eq}$ basically show the same sign in both hemispheres. Therefore, f_z is proportional to b_z and it results in a bulk acceleration of the PNS core. Analogously, the angular momentum exchange has a dependence on the direction of the toroidal magnetic field. Consequently, the antiparallel toroidal magnetic field between the northern and southern hemispheres seen in our magnetized models leads to the spin down and spin up, respectively. We mention that the sign of f_z can change with time, as we will show later, probably depending on the neutrino profiles H^μ as well as on u^μ in Equation (59).

In Figure 5, we depict the same values as in Figure 4, but for model R1B13 to see the outcomes of a one order of magnitude stronger initial magnetic field. From panels (a) and (b), the magnetic field is not showing a similar structure to that in model R1B12. For instance, B_z seems to consist of higher-order l modes. As already discussed in Section 5.1 and also will be shown in Figure 8 in Appendix B, less mass inflow along the equatorial plane might hinder the collimation effect of the outflow where it is launched. Consequently, the magnetic field at the base of the outflow might not be aligned with the rotational axis compared to that in R1B12. Aside from such difference seen in the magnetic field structure, the effects of modified neutrino−matter interactions are qualitatively the same as in R1B12. Reflecting the global magnetic field, whose direction is roughly tilted at an angle of $\sim -45^\circ$ from the rotational axis on the $y = 0$ plane (see panel a), the region with $z \gtrsim x$ shows, e.g., the excess of deleptonization and cooling rate, which is analogous to what we see in the northern hemisphere of model R1B12. The relative contribution of modified neutrino−matter interactions to the total ones is approximately several to $\sim$10% from panels (d)–(f), which is approximately one order of magnitude larger than that in model R1B12. This model with a different magnetic field structure from model R1B12 clearly shows the importance of magnetic field structure, which potentially determines the global pattern

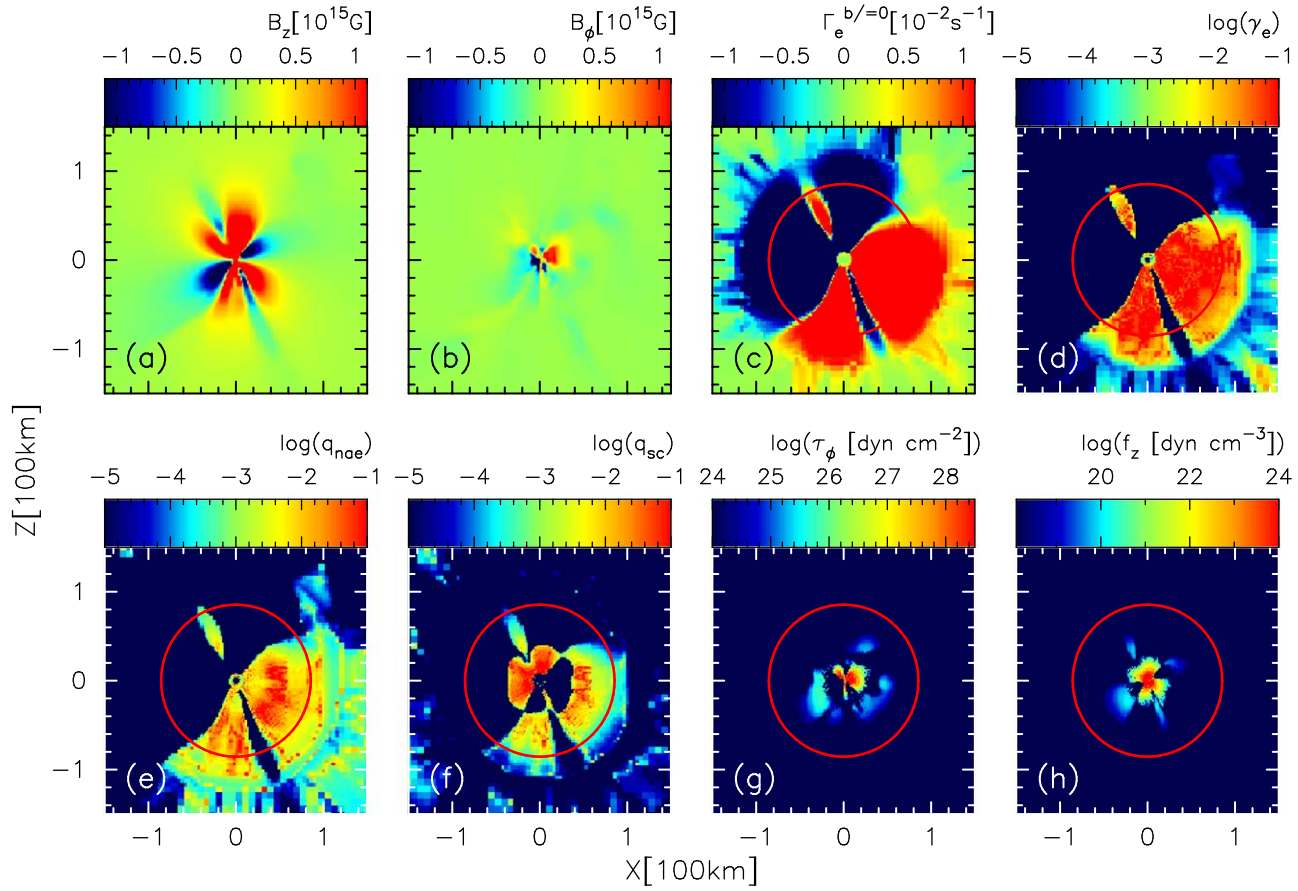

Figure 5. Same as Figure 4, but for model R1B13 at $t_{\rm pb} = 65$ ms.

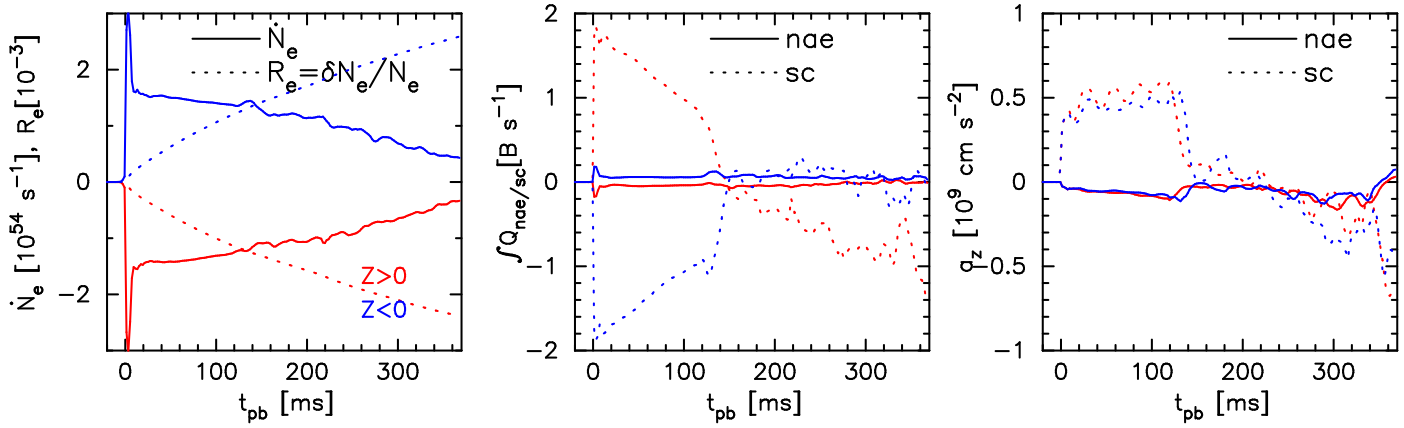

Figure 6. We show the deleptonization rate (left panel), energy deposition rate (middle), and acceleration of PNS a_z (right) in each hemisphere. See the text for their definitions. In the middle and right panels, the line style corresponds to the neutrino−matter interaction, either modified "nae" (solid) or "sc" (dashed) process.

of the parity-violation effect, and, thus, of the magnetohydrodynamic evolution in the PNS.

At the end of this section, we discuss the time evolution of the modified source terms and their cumulative impact on the PNS core. In Figure 6, we show the deleptonization rate (left panel), energy deposition rate (middle), and acceleration of PNS (right). To plot the left panel, we again introduce several quantities as follows: the total deleptonization rate due to the modified interactions

$$\dot{N}_e = \int dx^3 n_{\rm b} \Gamma_e^{b\neq 0} \tag{60}$$

and its cumulative value

$$\delta N_e = \int_{-\infty}^{t} dt \dot{N}_e, \tag{61}$$

number of electrons

$$N_e = \int dx^3 \rho^* Y_e, \tag{62}$$

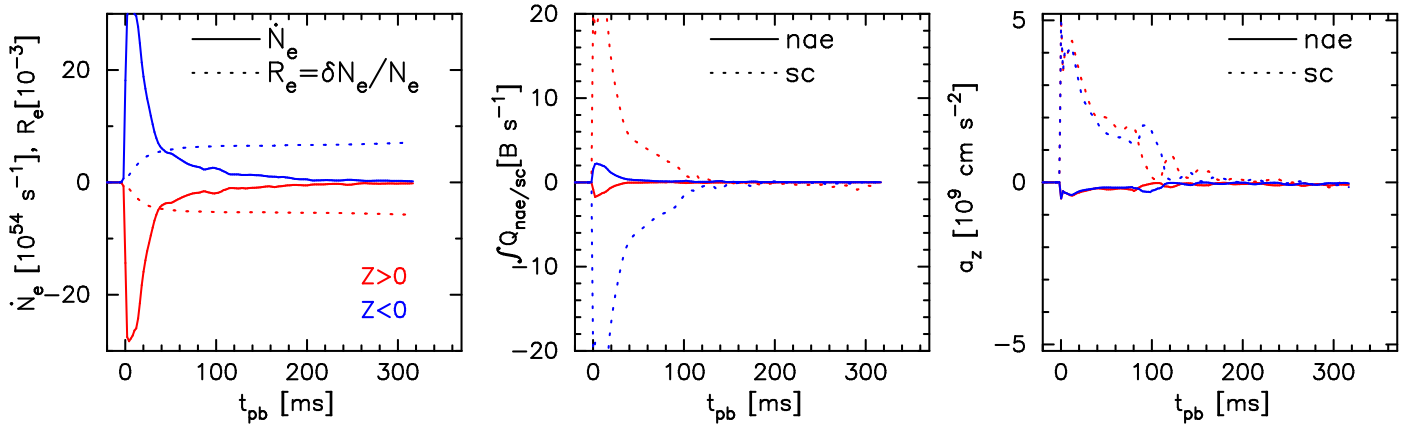

Figure 7. Same as Figure 6, but for model R1B13.

and the ratio R_e, which measures the degree of partial distribution of electrons inside the PNS,

$$R_e = \frac{\delta N_e}{N_e}. \tag{63}$$

The volume integral is performed for each hemisphere $z > 0$ (northern hemisphere, red lines) and $z < 0$ (southern hemisphere, blue) and also for the region with $\rho \geqslant 10^{12}$ g cm^{-3}. In the middle panel, the energy gain or loss in each hemisphere is evaluated by the volume integral of $Q^{b\neq 0}_{\rm nae/sc}$. In the right panel, we evaluate the z component of PNS acceleration a_z by

$$a_z = \frac{1}{M_{\rm PNS}} \int dx^3 f_z, \tag{64}$$

where $M_{\rm PNS} = \int dx^3 \rho^*$ is the PNS mass in each hemisphere. In both the middle and right panels, the solid and dashed lines indicate the contribution from modified neutrino absorption and emission (nae) and scattering (sc) processes, respectively.

From the left panel in Figure 6, the volume-integrated deleptonization rate in each hemisphere exhibits a clear asymmetry throughout the simulation time. $\dot{N}_e$ in the northern hemisphere reaches $\dot{N}_e \sim -10^{54}$ s^{-1} (red solid line), indicating more deleptonization there. Its cumulative value reaches $R_e \sim -0.2\%$ of the total electron number inside the PNS at the final time of simulation. Meanwhile, in the southern hemisphere, those values have the opposite sign, but with almost the same absolute values as those in the northern hemisphere. Therefore, the parity-violation effect can potentially produce a north–south asymmetry in Y_e of the order of a few per mille in this model. Regarding the energy deposition rate in the middle panel, significant energy transfer occurs mainly during the first hundred milliseconds after bounce. However, from panels (e) and (f) in Figure 4, the energy transfer due to these terms takes place mostly within the gain radius denoted by the red circle. We thus argue that the modified terms do not have a noticeable impact on the neutrino-heating explosion mechanism.

The apparent PNS acceleration a_z, which is simply evaluated from the source term of momentum exchange, shows a significant value of $\sim 5 \times 10^8$ cm s^{-2} and lasts $\sim$100 ms after bounce. We note that the momentum exchange through the normal neutrino−matter interaction processes without the influence of a magnetic field, i.e., via the term $S^{\alpha,b=0}_{\varepsilon}$ (Equation (43)), shows a nearly, not perfect, asymmetric property with respect to the equatorial plane. For instance, at $t_{\rm pb} = 50$ ms, a_z evaluated from $S^{\alpha,b=0}_{\varepsilon}$ reaches $\sim +7.1(-7.3) \times 10^{10}$ cm s^{-2} in the northern (southern) hemisphere, resulting in a nonvanishing net acceleration of $\sim -2 \times 10^9$ cm s^{-2}. We note that our nonrotating, nonmagnetized model R0B00 shows the net acceleration of $\sim 10^7$ cm s^{-2}, which is essentially zero. We thus consider that the nonvanishing acceleration contributed solely from $S^{\alpha,b=0}_{\varepsilon}$ originates from the asymmetric hydrodynamic background with respect to the equatorial plane. Anyway, we argue that the symmetric property seen in a_z evaluated from $S^{\alpha,b\neq 0}_{\varepsilon}$ (right panel in Figure 6) has a comparable influence to that from $S^{\alpha,b=0}_{\varepsilon}$. We also mention that we do not observe a meaningful PNS core kick during the simulation time. This is due to the relevant neutrinos still being trapped and not carrying away the momentum during the simulation time. It marginally shows a slight oscillation after $t_{\rm pb} \sim 100$ ms with the displacement of several hundred meters, possibly indicating the appearance of standing accretion shock instability (SASI; Foglizzo et al. 2006; Scheck et al. 2006). Another remarkable thing is that the modified scattering term is again the main contribution by comparing the dotted (sc) and solid (nae) lines in the middle and right panels.

In Figure 7, we plot the same figure as Figure 6, but for model R1B13 which employs a one order of magnitude larger initial magnetic field. We see a qualitatively similar trend to that of R1B12. Most of the lepton, energy, and momentum exchanges occur during the first $\sim$100 ms after bounce. However, compared to the values in model R1B12, all values plotted in Figure 7 show roughly one order of magnitude larger values. This is simply because the modified source terms employed (Equations (26) and (41)) have a linear dependence on the magnetic field b_μ.

6. Summary and Discussion

In this study, we have presented a formalization of the correction term of neutrino–matter interaction rates in the presence of external magnetic field. The formalism is based on Arras & Lai (1999), and we took into account the modified interaction rates of two major processes in the SN core: neutrino–nucleon scattering and neutrino absorption and emission processes. We extracted the zeroth- and first-order angular dependencies of the interaction rates and derived the source term suitable for the M1 neutrino transport in full relativity. The final expression of the source terms is described

in terms of the normal radiation moments. Because the magnetic potential energy of free electrons and nucleons, $\hbar ceb$ and $\mu_B b$, respectively, are significantly smaller than the matter temperature in typical MHD CCSN models, we can safely truncate the second- or higher-order terms in the magnetic field strength, leading to the source terms having a linear dependence on it. We also proved that the modified scattering term does not violate the lepton-number conservation, which is crucial to accurately follow the PNS deleptonization.

Utilizing state-of-the-art general relativistic M1 neutrino transport code with the gravitational red- and Doppler shift terms being fully considered, we have conducted MHD CCSN simulations of a 20 $M_\odot$ star (Woosley & Heger 2007). We calculated three models, nonrotating nonmagnetized (R0B00), rotating magnetized (R1B12), and rotating strongly magnetized (R1B13), to explore the effects of the progenitor's rotation and magnetic field both on the dynamics and the modified neutrino–matter interactions. For the nuclear EOS, we used the SFHo of Steiner et al. (2013). Other than the correction terms in neutrino–matter interactions due to the magnetic field, one of the major differences from our previous study (Kuroda et al. 2020) is that we used up-to-date neutrino opacities based on Kotake et al. (2018). We adopted the most elaborate electron capture rate on heavy nuclei following Juodagalvis et al. (2010). Furthermore, we also took into account the following: inelastic contributions and weak magnetism corrections (Horowitz 2002), the density-dependent effective nucleon mass (Reddy et al. 1999), the quenching of the axial-vector coupling constant (Carter & Prakash 2002; Fischer 2016), many-body and virial corrections (Horowitz et al. 2017), and strangeness contribution to the axial-vector coupling constant (Horowitz 2002). Investigating the impact of these up-to-date neutrino opacities will be reported elsewhere.

Concerning the dynamics, while no shock revival was observed in model R0B00 during our simulation time of ∼500 ms after bounce, the shock expansion initiated shortly after bounce in two magnetized models. We found essentially the same dynamical features between models R0B00/R1B12 in this study and their corresponding models in Kuroda et al. (2020). The only difference is that the bipolar explosion that appeared in model R1B12 in this study did not diminish, although it showed a slight asymmetry with respect to the equatorial plane. In model R1B13, we observed the most rapid shock expansion and largest increment of the explosion energy among the three models. However, the expansion speed of model R1B12 eventually seemed to be faster than that of model R1B13 at the final simulation time. The explosion energy in model R1B12 reached the value of $\sim 10^{50}$ erg, which is consistent with our previous study. The reason why the initially less magnetized model R1B12 eventually exhibited more energetic shock expansion originates from the larger mass accretion rate. In model R1B12, we witnessed significantly larger mass inflow and outflow rates than those in model R1B13. Compared to the case in R1B13, the prompt shock propagated significantly more slowly in model R1B12, which allowed nonaxisymmetric matter motion, e.g., one-armed spiral pattern, to fully develop. The spiral pattern could then produce a flow channel through which a noticeable amount of mass accretion took place, leading to more liberation of gravitational energy.

One of the aims of this study is to self-consistently assess the actual impact of modified neutrino–matter interaction rates on the lepton, energy, and momentum exchanges. In addition, we focused on the global asymmetry that could be induced by the initial dipole-like magnetic field employed in this study. From our results, we found a clear asymmetric feature in both the deleptonization and energy deposition rates with respect to the equatorial plane. As for the asymmetric deleptonization rate, the northern (southern) hemisphere lost more (fewer) electrons. The energy deposition rate through the modified neutrino absorption and emission process showed basically the same asymmetric feature as that of the deleptonization rate. These features can be understood to be the dependence of the corresponding source term on the inner product of the diffusion flux of neutrinos and the magnetic field. The sign of the inner product changes between the northern and southern hemispheres if the magnetic field is dominated by a dipole (or more precisely an odd l-mode) structure. We also demonstrated that a different magnetohydrodynamic evolution produces a different magnetic field structure within the shocked region leading to a different pattern of parity-violation effects.

The cumulative impact of the asymmetric deleptonization rate asymptotically reaches ∼0.1%–1%. Our result also indicates the importance of the modified inelastic scattering process, at least in the explosion phase, which has been often omitted in previous literature (Kotake et al. 2005; Suwa & Enoto 2014; Dobrynina & Ognev 2020). The energy deposition rate from the modified scattering term showed roughly a one order of magnitude larger value than the absorption process.

In contrast to the lepton and energy exchanges, the linear momentum exchange showed a symmetric property, e.g., the z component of the PNS acceleration showed the same sign and value in both hemispheres. Roughly speaking, such feature stems from the source term projected onto the Eulerian frame being parallel to the magnetic field. An initially dipolar-like magnetic field leads to a magnetic field configuration in the proto-magnetar composed of a nearly uniform z component and antiparallel toroidal field in both hemispheres. Therefore, both hemispheres gain acceleration in the same z direction, while there is a torsional effect between the two hemispheres.

In terms of scattering and absorption cross sections, we can summarize our results as follows: the scattering cross sections for neutrinos are enhanced (reduced) if neutrinos propagate parallel (antiparallel) to the magnetic field, which is consistent with the positive acceleration of the PNS core. On the contrary, the absorption cross sections are reduced (enhanced) if neutrinos propagate parallel (antiparallel) to the magnetic field, which is in line with, for instance, the smaller deleptonization rate, i.e., fewer neutrinos are captured, displayed in the northern hemisphere (see panel (c) in Figure 4). These trends in enhancement or reduction are consistent with the study of Maruyama et al. (2011, 2012).

We stress that most of the energy, leptons, and linear and angular momenta that are transferred through the modified source terms are not immediately taken away from deep inside the PNS core. We actually investigated if there is a noticeable north–south asymmetry in Y_e or the neutrino's energy and number fluxes on the PNS surface, though we could not find them with significance. Therefore, we conclude that the modified source terms do not play important roles in the dynamical timescale and contribute neither the explosion dynamics nor the natal ($t_{\rm pb} \lesssim 1$ s) PNS kick. This basically

agrees with previous studies by Kotake et al. (2005) and Dobrynina & Ognev (2020). However, once those trapped neutrinos diffuse out of the PNS core on a timescale of $\gtrsim\mathcal{O}(1)$ s, namely in the Kelvin–Helmholtz cooling phase, they can potentially produce a ∼0.1%–1% asymmetry in the PNS structure. Along with the neutrino diffusion, a partial distribution of Y_e may gradually appear, leading to a more pronounced asymmetric neutrino emission. In addition, the modified scattering and absorption processes themselves contribute to the globally asymmetric neutrino emission. The final outcome of the asymmetric neutrino signal depends on these two effects that definitely interact with each other. Therefore, the assessment of the degree of the final outcome is highly complex and cannot be simply extrapolated from our results. It can be explored only through a long timescale MHD simulation. Our numerical simulations, however, provide us, for the first time, with realistic values of the impact of a magnetic field on the neutrino–matter interactions in MRE scenario, albeit in the early postbounce phase and for a small number of models.

It is a pleasure to thank Almudena Arcones for her encouragement and support for this work and also for her useful comments and suggestions. I acknowledge Kei Kotake and Tomoya Takiwaki for fruitful discussions and the new neutrino opacities that they provided me. This research was supported by the ERC Starting Grant EUROPIUM-677912. Numerical computations were carried out on Cray XC50 at CfCA, NAOJ.

Appendix A
Lepton-number Conservation

It is informative to show that the correction term $S_{\rm sc}^{\alpha,b\neq0}(\varepsilon)$ does not violate the lepton-number conservation, i.e., the number of neutrinos does not change through the scattering process. This is equivalent to satisfying the following condition (see Equation (15) in Kuroda et al. 2016):

$$\int\frac{d\varepsilon}{\varepsilon}S_{\varepsilon,\rm sc}^{\alpha,b\neq0}u_\alpha=0 \tag{A1}$$

for every flavor of neutrino. As we mentioned, the source term in Equation (11) consists of the zeroth- and first-order angular moments. Regarding the number integral of the first-order moment of the source term, i.e., inserting Equation (21) in Equation (A1), it is zero by definition due to the orthogonality conditions $L^{\alpha\beta}u_\alpha=0$ and $h^{\alpha\beta}u_\alpha=0$. We mention that the scattering source term with no contribution from the magnetic field, Equation (12), analogously conserves the lepton number because of the condition $H^\alpha u_\alpha=0$.

Concerning the remaining zeroth-order term in Equation (15), its number integral also becomes zero. To show that, we first rewrite Equation (15). After some manipulation, it becomes

$$\begin{aligned}&\varepsilon^3u^\alpha\int d\Omega B_{\rm sc}^{b\neq0}(\varepsilon,\Omega)\\&=2\pi u^\alpha\Bigg[\int d\mu'\int d\varepsilon'\left(\delta A_+DH_\varepsilon^\beta-\left(\frac{\varepsilon}{\varepsilon'}\right)\delta A_+{}'D'H_{\varepsilon'}^\beta\right)\\&+\int d\mu'\mu'\int d\varepsilon'\left(-\delta A_+{}'C'H_\varepsilon^\beta+\left(\frac{\varepsilon}{\varepsilon'}\right)\delta A_+CH_{\varepsilon'}^\beta\right)\Bigg]\hat b_\beta.\end{aligned} \tag{A2}$$

Here, we omit the argument $(\varepsilon,\varepsilon')$ in C and D for simplicity. In addition, C', D', and $\delta A_+{}'$ with a prime denote that the value of the incoming neutrino energy ε and that of the outgoing one ε' are switched, e.g., $\delta A_+'\equiv\delta A_+(\varepsilon',\varepsilon,\mu',b)$. For δA_+, this manipulation obviously does not alter the scattering angle μ' and magnetic field strength b. Furthermore, we also use the following relations:

$$q_0'=-q_0 \tag{A3}$$

$$D'=-e^{q_0/T}C \tag{A4}$$

$$\varepsilon'^2\delta A_+'C'=-\varepsilon^2\delta A_-D \tag{A5}$$

$$\varepsilon'^2\delta A_+'D'=-\varepsilon^2\delta A_-C. \tag{A6}$$

Consequently, the number integral of Equation (A2) results in

$$\begin{aligned}&\int\frac{d\varepsilon}{\varepsilon}u_\alpha\left(\varepsilon^3u^\alpha\int d\Omega B_{\rm sc}^{b\neq0}(\varepsilon,\Omega)\right)=-2\pi\hat b_\beta\\&\times\Bigg[\int d\mu'\int d\varepsilon d\varepsilon'\left(\frac{1}{\varepsilon}\delta A_+DH_\varepsilon^\beta-\frac{1}{\varepsilon'}\delta A_+{}'D'H_{\varepsilon'}^\beta\right)\\&+\int d\mu'\mu'\int d\varepsilon d\varepsilon'\left(-\frac{1}{\varepsilon}\delta A_+{}'C'H_\varepsilon^\beta+\frac{1}{\varepsilon'}\delta A_+CH_{\varepsilon'}^\beta\right)\Bigg]\\&=0.\end{aligned} \tag{A7}$$

Therefore, the condition in Equation (A1) is indeed satisfied for ν_e and analogously for $\bar\nu_e$, as we only have to replace δA_+ and $\delta A_+'$ in Equation (A7) by δA_- and $\delta A_-'$, respectively, for $\bar\nu_e$.

Appendix B
Explosion Dynamics of the Supplement Model R1B13

In this appendix, we briefly explain the explosion dynamics of a supplement model R1B13. After bounce, this model exhibits an approximately one order of magnitude larger magnetic field strength with a significantly different structure from a simple dipole-like one seen in model R1B12. We therefore consider this model as an appropriate one to see how the magnetic field structure determines the global pattern of parity-violation effects. In Figure 8, we show the same figure as Figure 1, but for model R1B13 at $t_{\rm pb}=185$ ms and at the final simulation time $t_{\rm pb}=316$ ms. The remarkable difference from model R1B12 is the absence of a clear bipolar structure. For instance, from 2D contours in the bottom panels, the outermost shock surface located at $R\sim4000$ km is more roundish, and the axis ratio is closer to unity than that of model R1B12. Inside the shocked region, the high-entropy region with $s\sim15\,k_{\rm B}$ baryon^{-1} appears, although the value is relatively low compared to model R1B12 throughout the computation. In addition, the entropy structure shows a small-scale and fragmented structure that is completely different from the global-scale high-entropy bipolar structure seen in model R1B12. Another remarkable feature is that the high-entropy blobs (e.g., yellowish region in the top two panels) are randomly oriented and basically not in alignment with the rotational axis in contrast to model R1B12. Reflecting such a feature, the magnetic field also exhibits a more stochastic structure, as can be partly understood from the plasma β (in the lower right panels of Figure 8), than that of model R1B12, which, in contrast, shows a bipolar structure consisting of high-plasma β gas.

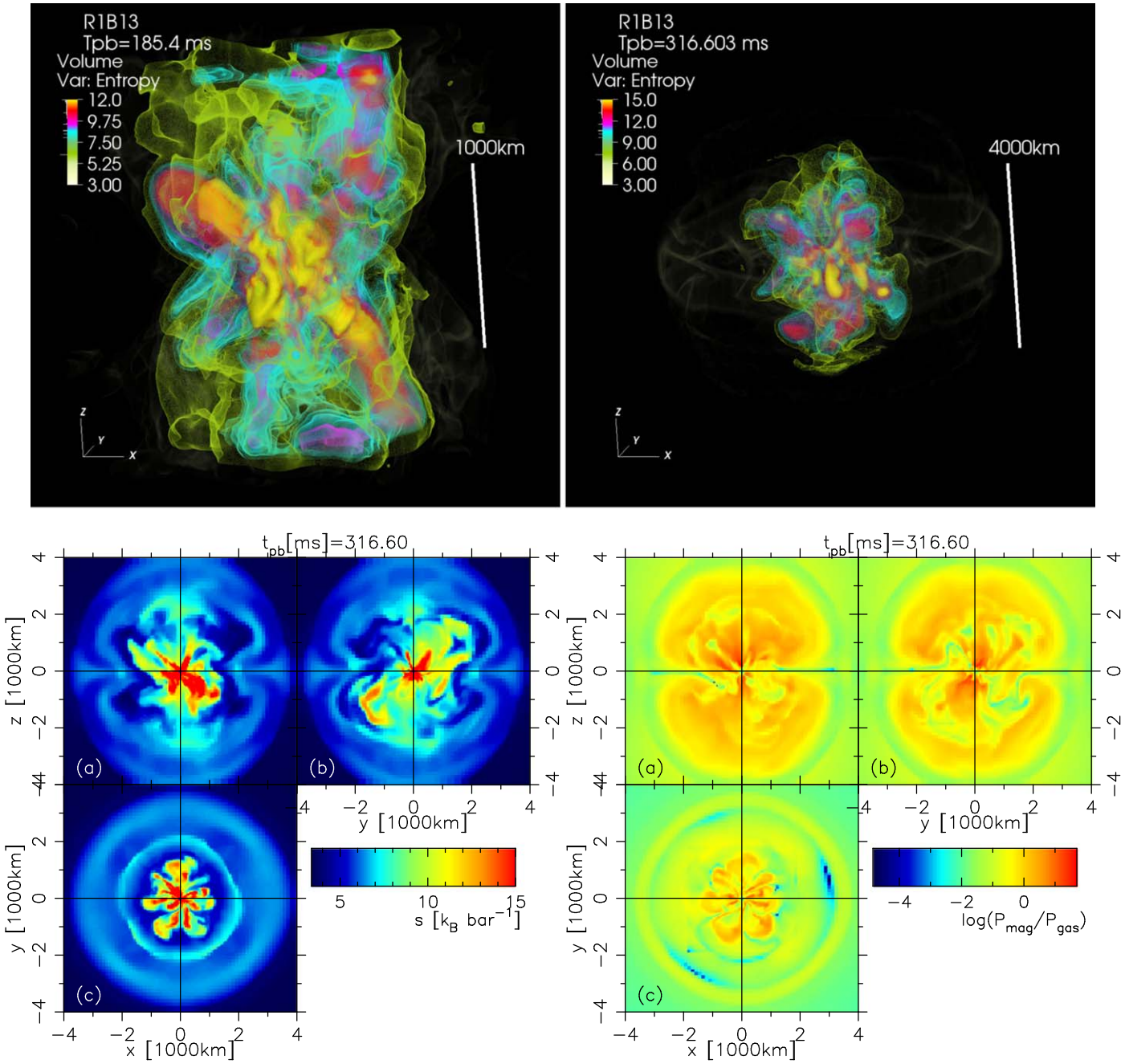

Figure 8. Same as Figure 1, but for model R1B13.

We consider that the reason for this random orientation is due to the absence of continuous magnetic field amplification, particularly the winding amplification along the rotational axis. As will be explained later, this model shows a lower mass accretion rate, and the winding mechanism, which requires a high mass accretion rate with angular momentum, does not operate. Due to the lack of a strong toroidal magnetic field along the rotational axis, the matter is not preferentially ejected along the rotational axis. In addition, there might be another possible reason for the misalignment, which is the tilt of the rotational axis. Although it is not the scope of this work to investigate in detail if the rotational axis tilts in model R1B13, from very recent full 3D MHD models in Obergaulinger & Aloy (2020b), the rotational axis, as well as the orientation of the outflow, can tilt due to asymmetric matter accretion onto the PNS. We found that the main mass accretion in model R1B13 takes place not only along the equatorial plane but also in all directions. It significantly differs from that of model R1B12, which shows a continuous accretion channel mainly along the equatorial plane. Although Obergaulinger & Aloy (2020b) reported the tilt of the rotational axis in their most weakly magnetized model, the absence of continuous mass accretion along the equatorial plane is a common feature seen in our model R1B13 and theirs.

ORCID iDs

Takami Kuroda https://orcid.org/0000-0001-5168-6792

References

Ardeljan, N. V., Bisnovatyi-Kogan, G. S., & Moiseenko, S. G. 2000, A&A, 355, 1181
Arras, P., & Lai, D. 1999, PhRvD, 60, 043001
Begelman, M. C. 1998, ApJ, 493, 291
Bisnovatyi-Kogan, G. S. 1970, AZh, 47, 813
Bisnovatyi-Kogan, G. S. 1993, A&AT, 3, 287
Bruenn, S. W. 1985, ApJS, 58, 771
Bruenn, S. W., Lentz, E. J., Hix, W. R., et al. 2016, ApJ, 818, 123
Bugli, M., Guilet, J., Obergaulinger, M., Cerdá-Durán, P., & Aloy, M. A. 2020, MNRAS, 492, 58
Burrows, A., Dessart, L., Livne, E., Ott, C. D., & Murphy, J. 2007, ApJ, 664, 416
Carter, G. W., & Prakash, M. 2002, PhLB, 525, 249
Chan, C., Müller, B., Heger, A., Pakmor, R., & Springel, V. 2018, ApJL, 852, L19
Dobrynina, A., & Ognev, I. 2020, PhRvD, 101, 083003
Duncan, R. C., & Thompson, C. 1992, ApJL, 392, L9
Ezzeddine, R., Frebel, A., Roederer, I. U., et al. 2019, ApJ, 876, 97
Fischer, T. 2016, A&A, 593, A103
Foglizzo, T., Scheck, L., & Janka, H.-Th. 2006, ApJ, 652, 1436
Gessner, A., & Janka, H.-T. 2018, ApJ, 865, 61
Glas, R., Janka, H. T., Melson, T., Stockinger, G., & Just, O. 2019, ApJ, 881, 36
Hannestad, S., & Raffelt, G. 1998, ApJ, 507, 339
Heger, A., & Langer, N. 2000, ApJ, 544, 1016
Hobbs, G., Lorimer, D. R., Lyne, A. G., & Kramer, M. 2005, MNRAS, 360, 974
Horowitz, C. J. 2002, PhRvD, 65, 043001
Horowitz, C. J., Caballero, O. L., Lin, Z., O'Connor, E., & Schwenk, A. 2017, PhRvC, 95, 025801
Horowitz, C. J., & Li, G. 1998, PhRvL, 80, 3694
Janka, H.-T. 2017, ApJ, 837, 84
Janka, H.-T., Melson, T., & Summa, A. 2016, ARNPS, 66, 341
Juodagalvis, A., Langanke, K., Hix, W. R., Martínez-Pinedo, G., & Sampaio, J. M. 2010, NuPhA, 848, 454
Katsuda, S., Morii, M., Janka, H.-T., et al. 2018, ApJ, 856, 18
Kotake, K., Takiwaki, T., Fischer, T., Nakamura, K., & Martínez-Pinedo, G. 2018, ApJ, 853, 170
Kotake, K., Yamada, S., & Sato, K. 2005, ApJ, 618, 474
Kumar, P., & Zhang, B. 2015, PhR, 561, 1
Kuroda, T., Arcones, A., Takiwaki, T., & Kotake, K. 2020, ApJ, 896, 102
Kuroda, T., Takiwaki, T., & Kotake, K. 2016, ApJS, 222, 20
Lai, D. 2001, in Neutron Star Kicks and Asymmetric Supernovae, ed. D. Blaschke, N. K. Glendenning, & A. Sedrakian, Vol. 578 (Berlin: Springer), 424
LeBlanc, J. M., & Wilson, J. R. 1970, ApJ, 161, 541
MacFadyen, A. I., & Woosley, S. E. 1999, ApJ, 524, 262
Mandel, I. 2016, MNRAS, 456, 578
Maruyama, T., Hidaka, J., Kajino, T., et al. 2014, PhRvC, 89, 035801
Maruyama, T., Kajino, T., Yasutake, N., Cheoun, M.-K., & Ryu, C.-Y. 2011, PhRvD, 83, 081303
Maruyama, T., Yasutake, N., Cheoun, M.-K., et al. 2012, PhRvD, 86, 123003
Meier, D. L., Epstein, R. I., Arnett, W. D., & Schramm, D. N. 1976, ApJ, 204, 869
Metzger, B. D., Giannios, D., Thompson, T. A., Bucciantini, N., & Quataert, E. 2011, MNRAS, 413, 2031
Mösta, P., Richers, S., Ott, C. D., et al. 2014, ApJL, 785, L29
Müller, B. 2016, PASA, 33, e048
Müller, B., Gay, D. W., Heger, A., Tauris, T. M., & Sim, S. A. 2018, MNRAS, 479, 3675
Müller, B., Melson, T., Heger, A., & Janka, H.-T. 2017, MNRAS, 472, 491
Müller, B., Tauris, T. M., Heger, A., et al. 2019, MNRAS, 484, 3307
Müller, E., & Hillebrandt, W. 1979, A&A, 80, 147
Nagakura, H., Sumiyoshi, K., & Yamada, S. 2019, ApJL, 880, L28
Nakamura, K., Kuroda, T., Takiwaki, T., & Kotake, K. 2014, ApJ, 793, 45
Nakamura, K., Takiwaki, T., & Kotake, K. 2019, PASJ, 71, 98
Nomoto, K., Tominaga, N., Umeda, H., Kobayashi, C., & Maeda, K. 2006, NuPhA, 777, 424
Obergaulinger, M., & Aloy, M. Á. 2020a, MNRAS, 492, 4613
Obergaulinger, M., & Aloy, M.-Á. 2020b, arXiv:2008.07205
O'Connor, E. P., & Couch, S. M. 2018, ApJ, 865, 81
Ott, C. D., Roberts, L. F., da Silva Schneider, A., et al. 2018, ApJL, 855, L3
Pan, K.-C., Liebendörfer, M., Couch, S. M., & Thielemann, F.-K. 2018, ApJ, 857, 13
Powell, J., & Müller, B. 2019, MNRAS, 487, 1178
Proga, D., MacFadyen, A. I., Armitage, P. J., & Begelman, M. C. 2003, ApJL, 599, L5
Radice, D., Abdikamalov, E., Ott, C. D., et al. 2018, JPhG, 45, 053003
Reddy, S., Prakash, M., Lattimer, J. M., & Pons, J. A. 1999, PhRvC, 59, 2888
Repetto, S., Davies, M. B., & Sigurdsson, S. 2012, MNRAS, 425, 2799
Sawai, H., Kotake, K., & Yamada, S. 2008, ApJ, 672, 465
Sawai, H., & Yamada, S. 2016, ApJ, 817, 153
Scheidegger, S., Käppeli, R., Whitehouse, S. C., Fischer, T., & Liebendörfer, M. 2010, A&A, 514, A51
Scheck, L., Kifonidis, K., Janka, H.-Th., & Müller, E. 2006, A&A, 457, 963
Shibata, M., Kiuchi, K., Sekiguchi, Y., & Suwa, Y. 2011, PThPh, 125, 1255
Steiner, A. W., Hempel, M., & Fischer, T. 2013, ApJ, 774, 17
Summa, A., Janka, H.-T., Melson, T., & Marek, A. 2018, ApJ, 852, 28
Suwa, Y., & Enoto, T. 2014, MNRAS, 443, 3586
Takiwaki, T., Kotake, K., & Sato, K. 2009, ApJ, 691, 1360
Takiwaki, T., Kotake, K., & Suwa, Y. 2016, MNRAS, 461, L112
Tamborra, I., Hanke, F., Janka, H.-T., et al. 2014, ApJ, 792, 96
Vartanyan, D., Burrows, A., Radice, D., Skinner, M. A., & Dolence, J. 2019, MNRAS, 482, 351
Wang, T., & Burrows, A. 2020, PhRvD, 102, 023017
Winkler, P. F., & Petre, R. 2007, ApJ, 670, 635
Winteler, C., Käppeli, R., Perego, A., et al. 2012, ApJL, 750, L22
Wongwathanarat, A., Janka, H. T., & Müller, E. 2013, A&A, 552, A126
Woosley, S. E., & Heger, A. 2007, PhR, 442, 269